Karlsruhe Institute of Technology

Application of reverse-time migration for ultrasound medical imaging. Anwendung von Reverse-Time Migration zur medizinischen Ultraschall Bildgebung

Bachelor's Thesis of

Nico Heinz

at the Department of Physics
Institute for Geophysics

Reviewer:	Prof. Bohlen
Second reviewer:	Dr. Hertweck
Advisor:	M.Sc. F. Kühn

01. April 2018 – 26 September 2018

Karlsruher Institut für Technologie
Fakultät für Informatik
Postfach 6980
76128 Karlsruhe

I declare that I have developed and written the enclosed thesis completely by myself, and have not used sources or means without declaration in the text.

PLACE, DATE

. . . . . .

(Nico Heinz)

Deutsche Zusammenfassung

In Deutschland sterben jährlich über 18.000 Frauen in Deutschland an Brustkrebs. Dabei ist eine frühe Diagnoses einer der entscheidenden Faktoren für den Erfolg einer Therapie. Eine vielversprechende, sich in der Entwicklung befindliche Diagnose-Technolgie ist das Abbilden der Brust mit Ultraschall. Hierbei werden akustische Wellen durch die Brust der Frau gesendet und anschließend mit mehreren Empfängern aufgezeichnet. Aus den gemessenen Daten lässt sich daraufhin die Schallgeschwindigkeitsverteilung innerhalb der Brust rekonstruieren (Tomografie) und die Gewebegrenzen abbilden (Migration). Migrationsmethoden setzen ist ein bekanntes Geschwindigkeitsmodell voraus. Während bereits einige Prototypen der Scanner entwickelt sind, bereitet die Bildrekonstruktion noch Schwierigkeiten.
Die momentan bedeutenste Migrationsmethode ist die Synthetic Aperture Focusing Technik (SAFT). SAFT verwendet eine Strahlennäherung der Ultraschallwellen und vernachlässigt dadurch viele Wellenphänomene. Eine Berücksichtigung dieser Phänomene könnte das Ergebnis der Migration verbessern. Dies ist mit Reverse-Time Migration möglich. Bei dieser Migrationsmethode wird zunächst das vorwärtspropagierende Wellenfeld und anschließend das von den gemessenen und in der Zeit umgekehrten Seismogrammen verursachte, rückwärts propagierende Wellenfeld simuliert. Die Kreuzkorrelation dieser beiden Wellenfelder und Summation über alle Zeitschritte, Empfänger und Sender führt zu einem Abbild der Reflektoren. Die Wellenfelder können beispielsweise mittels der Methode der Finiten Differenzen berechnet werden, allerdings bedeuted die Lösung der Wellengleichung einen sehr hohen Rechenaufwand und damit hohe Anforderungen an die IT-Infrastruktur.
Reverse-Time Migration ist ein in der Geophysik angewandtes, in der medizinischen Technik jedoch noch nicht näher beachtetes Verfahren. Roy et al. (2016) führten die erste veröffentlichte Studie zu Reverse-Time Migration im medizinischen Kontext durch. Sie zeigen anhand numerischer Tests, dass mit diesem Verfahren die weibliche Brust abgebildet werden kann. Bei den Experimenten wird der Einfluss des medizinischen Messumfeldes noch nicht berücksichtigt. Beispielsweise wird die Bildgebung durch die mögliche Bewegung des Patienten während der Datenaufnahme, Rauschen in den Messdaten und Unsicherheiten im Geschwindigkeitsmodell erschwert. Der Einfluss dieser Faktoren ist noch nicht bekannt.

Das Ziel dieser Arbeit ist, anhand numerischer Experimente Probleme für die Bildgebung mit Reverse-Time Migration im medizinischen Messumfeld zu untersuchen und Lösungsmöglichkeiten zu entwickeln oder vorzuschlagen.

Hierzu werden zunächst aus dem in obiger Abbildung dargestellen Modell synthetische Seismogramme berechnet. Die Seismogramme werden zunächst mit dem gleichen Modell

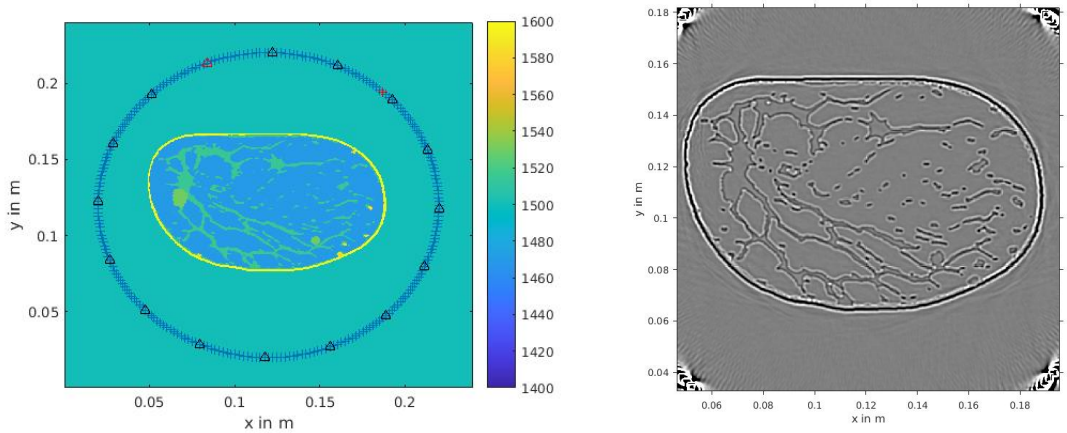

Links: Ergebnis der Reverse-Time Migration nach Anwenden des Laplace-Filters.
Rechts: Reverse-Time Migration mit entfernter direkter Welle.

migriert. Das Ergebnis der Migration wird durch Entfernen der direkten Welle aus den Seismogrammen und einen Laplace- Bildfilter verbessert. Das Ergebnis ist in obiger Abbildung dargestellt. Ein folgender direkter Vergleich mit einer SAFT-Migration zeigt, dass Reverse-Time Migration deutlich schärfere, kontrastreichere und artefaktärmere Bilder produziert.

Weitere Experimente ergeben, dass Reverse-Time Migration sehr robust gegenüber Fehler im Geschwindigkeitsmodell ist. Zwar ist eine Migration mit einer konstanten Geschwindigkeit für die Zielanwendung nur unzureichend scharf, doch reicht bereits ein mit einem strahlenbasierten Verfahren erstelltes Modell, um mit Reverse-Time Migration ein scharfes Abbild der Reflektoren zu erhalten.
Die Stabilität von Revere-Time Migration gilt auch gegenüber verrauschten Messdaten. Noch bis zu einem Signal-zu-Rausch Verhältnis von nur 4 dB sind nahezu alle Strukturen in der Brust lokalisierbar. Weitere Versuche lassen vermuten, dass das Rauschen in den Bildern mit $1/\sqrt{\text{Anzahl der Sender}}$ abnimmt. Durch Entfernen der direkten Welle aus den Seismogrammen wird das Ergebnis bei verrauschten Seismogrammen noch einmal deutlich verbessert.
Allerdings ist Reverse-Time Migration sehr empfindlich gegenüber Bewegungen der Brust während der Datanaquisition. Bereits Verschiebungen von etwa 2 mm verursachen solch starke Bewegungsartefakte im Bild, das eine nähere Beschreibung von dessen Strukturen unmöglich ist. Das Lösen dieses Problems ist die Voraussetzung für eine klinische Anwendung. Da ein einzelnes Wellenfeld nur wenige Zehntel Millisekunden braucht, um durch die Brust zu den Empfängern zu laufen, sind die einzelnen Schüsse kaum durch Bewegung beeinflusst und eine numerische, geometrische Korrektur der Position der Brust vor den einzelnen Schüssen reduziert vermutlich die meisten Bewegungsartefakte.

Zusammenfassend konnte gezeigt werden, dass Reverse-Time Migration im medizinischen Messumfeld möglicherweise die beste Ultraschall-Migrationstechnik ist, vorausgesetzt die notwendigen hohen Rechenkapazitäten sind verfügbar.

Abstract

Every year, more than 18 000 women in Germany die of breast cancer. An early diagnosis is an important factor for a successful treatment. A promising diagnostic technique is ultrasound imaging, but its development still faces some difficulties, such as the image reconstruction.
Reverse-time migration is a possible method to compute images of the acoustic reflectors inside a medium, which requires an available velocity model of the mediums. To the author's best knowledge, besides a study of Roy et al. (2016), this algorithm has not been recognized in medical imaging yet. They show by numerical experiments that the female breast can be depicted with this migration method. These first experiments neglect the influence of the medical measurement environment on the data acquisition and migration yet.
The purpose of this study is to identify possible problems regarding the measurement environment and to find or propose solutions to these problems. Therefore it is examined to what extend the movement of the body during the data acquisition and noise in the seismic data affect the migration. Another important question is how precise the velocity and density models have to be and how they can be obtained.

Acknowledgements

A very special gratitude goes out to Thomas Hertweck and Fabian Kühn from the Geophysical Institute, who have provided great support and supervision in the working process. Thank you, our talks about science and seismics have always been an enrichment, too. The doors to your offices have always been open whenever I ran into a trouble spot or had a question about my research or writing.
Thank you Fabian, too, for making the snapshots of the wavefields (figure 4.4).

Furthermore, I want to thank Prof. Thomas Bohlen for finding the idea of this work.

With a special mention to Torsten Hopp from the institute of process control systems and electronics for making the SAFT migration (figure 4.9), which makes it possible to directly compare SAFT to reverse-time migration.
I also want to thank Nicole Ruiter for teaching me about ultrasound technique.

I am also grateful to everybody who has been involved in my education within the recent years, especially from the geophysical institute, for a very pleasant, enriching and supportive study atmosphere.

And finally, last but by no means least, I have to express my very profound gratitude to my parents Sandra and Arnold and the rest of my family, for providing me with unfailing support and continuous encouragement throughout my years of study and my whole lifetime.

Contents

List of Figures

List of Tables

1. Introduction

Over 70 000 times a year, doctors in Germany make the diagnosis breast cancer. Among women, breast cancer has a share of about one third of all diagnosed cancers (Rhiem and Schmutzler, 2015). Statistics by the Robert Koch Institut (2018) reveal that breast cancer has been the death reason for over 18 000 women in Germany in 2015.
An early diagnosis is one important factor for successful treatment. According to statistics published by the American Cancer Society (2009) approximately 61% of all women in the United States are found to have localized breast cancers at the time of diagnosis. They have a 5-year survival rate of 98%. The later the cancer is diagnosed the more the survival rate declines. If the cancer is diagnosed with distant metastases, the survival rate is lowered to only 23% (Duric and Littrup, 2018).
These numbers prove that breast cancer is an important issue and research on it is a chance to increase life expectancy and health. As Aiello et al. (2004) point out, early recognition can reduce the mortality by around 25%, which motivates the development of better diagnosis techniques.

Chapter 2 starts with a discussion of traditional breast cancer diagnostic techniques such as X-ray based mammography or magnetic resonance imaging. They have some disadvantages, for instance radiation exposure or high economic costs (Spiegel Online, 2017). Ultrasound technique is a promising alternative. It can potentially make high-resolution three-dimensional images and might be a reasonable method for mass screening since it is uncomplicated in the application and cheap. However, it is still at development stage due to difficulties in the reconstruction technique (Ozmen et al., 2015).
One possibility is tomography, which aims at finding a velocity model of the subsurface. There exist a number of high-resolution and precise iterative tomography algorithms such as contrast-source inversion or full-waveform inversion (Ozmen et al., 2015). Unfortunately, their high computational cost hampers their reasonable field application in ultrasound medical imaging because the computation of the image should be finished within some minutes, which is currently not possible. Alternative, faster algorithms such as the bent ray reconstruction have an insufficient resolution for breast cancer detection (Hormati et al., 2010).
In contrast to tomography, migration only tries to localize the position of the acoustic reflectors. Migration requires an available velocity model. An exemplary algorithm is the synthetic aperture focusing technique (Hardt et al., 2012), in Geophysics also known as Kirchhoff migration. This algorithm neglects many wave phenomena, and taking account of these phenomena can possibly improve the image quality. One such technique is reverse-time migration.
This method uses the cross-correlation of a simulated source and receiver wavefield to compute an image (Claerbout, 1981). The simulation can be implemented, for instance,

with the method of finite elements. Sinces reverse-time migration produces different image artifacts, methods are discussed how these artifacts can be removed from the image. Besides the work of Roy et al. (2016), to the author's best knowledge, no other study on reverse-time migration for ultrasound medical imaging has been published so far. The group shows by means of numerical experiments on a model that reverse-time migration is capable to depict the female breast. The experiments neglect the medical measurement environment, and the effect of these conditions, including, for instance, the movement of the patient during the data acquisition, is not known yet.
The purpose of this study is to determine in numerical experiments how the measurement conditions as they occur in medical imaging affect the capability of reverse-time migration to map the female breast (chapter 4). This way, possible problems are analyzed in order to find or propose solutions to these problems. For example, the patient might move during the data acquisition. Consequently, the body movement is simulated in order to find its effect on reverse-time migration. Furthermore, the measured data are contaminated with noise. The robustness of reverse-time migration against noise in the seismic data is evaluated. Moreover, it is determined how uncertainties in the model affect the migration result and which tomography algorithm is useful to obtain the required velocity model. A comparison of the migration result with the image obtained with the synthetic aperture focusing technique allows to directly estimate the effect of wave phenomena on the migration.

2. Breast cancer detection

More than 40% of all tumors in the female breast in the United States are detected by the women themselves by feeling or seeing (Roth et al., 2011). These cancers are already at advanced stage and have a median size of $2 - 2.5$ mm (Guth et al., 2008). Unfortunately palpable cancers are inherently different from nonpalpable cancers, with a less diffusive growth pattern, more abnormalities and a worse prognosis (Skinner et al., 2001). This means that other diagnostic techniques are necessary that allow to make an earlier diagnosis.

2.1. Mammography

One such technique is mammography. In mammography, X-rays are sent through the breast and attenuated differently due to various structures like muscles, conjunctive tissue or tumors. On the other side of the breast a detector registers the radiation, building an image with shadows of the structures inside. This method can detect very small changes and allow an early diagnosis. The median size of breast cancers at the time of diagnosis amounts to $1 - 1.5$ mm (Guth et al., 2008). The dose of radiation used for a screening mammogram of both breasts amounts to about 0.4 mSv, which equals the natural radiation of about seven weeks. Unlike in nature, only the breast is exposed to the radiation and other parts of the body are not affected. Strong improvements in detector sensibility within the last years are the reason for the relatively low radiation dose (American Cancer Society, 2009). Due to a guideline published by the university hospitals Gießen and Marburg, mammography is the only procedure being generally accepted for the detection of young cancers (Albert et al., 2008). In Germany, a general screening program has been introduced for woman between 50 to 69 years old. They have a right to a mammography every two years (Gemeinsamer Bundesausschuss, 2017).
Nevertheless, this technique is not the perfect instrument for general diagnosis. Mammography compresses the breast before X-raying it, which makes its results unrepeatable and can be painful for the women. The sensitivity of mammography is greatly reduced for women with dense breast tissue or with a pronounced mastopathy (Duric and Littrup, 2018). After a radiotherapy this method is not recommended either due to the radiation exposure. Pregnant women should inform their doctors first. Another problem regarding mammography is a large number of false positives. They can cause anxiety and the following extra tests cost time and money. Hence additional alternative imaging techniques are helpful (Amstrong et al., 2007).

2.2. Magnetic resonance imaging

Protons, the cores of hydrogen, which can be found in water and fat molecules, have an intrinsic angular momentum, the spin. If they are excited in a magnetic field their rotation axis rotates, a phenomenon that is called precession, with a specific frequency, the lamor frequency. A second magnetic field that alternates with the same frequency can tilt the protons. After switching the alternating field off, the protons will move back to their original orientation. This reorientation is accompanied with the emitting of electromagnetic waves (Liang and Lauterbur, 1999). The described physical phenomenon can be used for medical imaging by putting the patient into an adapted field. Measuring the electromagnetic waves allows to recalculate their origin (Liang and Lauterbur, 1999). The main disadvantage of this technique is its high economical expense. One screening of the breast costs between 400 and 800 Euro. Therefore, it is too expensive to be applicable for mass screening (Spiegel Online, 2017).

2.3. Ultrasound imaging

Ultrasound imaging is based on the measurement of the traveltime of acoustic waves traveling through a medium, where they can be reflected and transmitted at discontinuities. A source emits an acoustic wave. Then the transmitted and reflected waves are registered. The traveltime from source to receiver, the wave's amplitude and its form can be used to determine the position of the reflectors. The shape of the reflectors and, depending upon the reconstruction algorithm, the speed of sound can indicate cancerous tissue. Recent studies have proven that the usage of ultrasound technique can almost double the cancer detection rate in denser breasts (Sehgal et al., 2006). This technology has no known side effects.

2.3.1. The physics of ultrasound

The equations of motion in a medium state that its momentum, which is the product of density $\rho(\vec{x}, t)$, the displacement $\vec{s}(\vec{x}, t)$ and the displacement velocity $\vec{v}(\vec{x})$ at the position $\vec{x}$ and time t can be changed by forces. Let i, j denote the ith and jth component of the vectors. Then, the forces are described by the stress tensor $\sigma_{ij}(\vec{x}, t)$ and body forces $\vec{f}(\vec{x}, t)$. The stress tensor σ_{ij} consists of nine components that completely define the state of stress at a point inside a material in the deformed state. In the case of medical ultrasound, the body force $\vec{f}$ is caused by impulses of the transmitters.

$$\rho \frac{\partial v_i}{\partial t} = \rho \frac{\partial^2 s_i}{\partial t^2} = \frac{\partial \sigma_{ij}}{\partial s_j} + f_i \tag{2.1}$$

The equation 2.1 is a second-order partial differential equation. Its solution describes the propagation of acoustic waves in the medium (Müller, 2007). Many works and implementations use the pressure $p = -\rho c^2 div\ \vec{s}$ instead of the displacement $\vec{s}$ (United States Naval Academy, 2017). Every time the acoustic impedance Z in the material changes, a part of

Table 2.1.: Approximate density in kg/m^3, velocity in m/s and impedance in 10^6 kg/m^2 s of different structures in the body at body temperature and normal ambient pressure. (Fledmann et al., 2009; Rumack et al., 2011)

medium	v	ρ	Z	reflected amplitude at muscle
air	331	1.3	0.00043	0.999
water	1500	1000	1.5	0.063
fat	1450	952	1.38	0.101
muscle	1580	1075	1.69	0

Table 2.2.: Thickness of biological tissues in cm required to attenuate the intensity (power) of an ultrasound beam by half (-3 dB) (Amin, 1989).

medium	1 MHz	2 MHz	5 MHz
air	0.25	0.06	0.01
water	1360	340	54
fat	5	2.5	1
muscle	1.5	0.75	0.3

the wave is being reflected. The impedance Z depends upon the material density ρ and the speed of sound v and can be calculated as

$$Z = \rho \, |\vec{v}| \tag{2.2}$$

where $|\cdot|$ denotes the length of a vector. The proportion of energy being reflected is called the reflection coefficient R. If a plane wave in the medium 1 reaches the interface to a second medium 2 orthogonally, the reflection coefficient equals

$$R = \frac{Z_2 - Z_1}{Z_1 + Z_2}. \tag{2.3}$$

Only a small amount of the source energy reaches the receivers due to acoustic absorption, scattering and reflection. Most of the energy is lost due to acoustic absorption. The acoustic intensity I after a distance d depends upon the absorption and scattering coefficient μ:

$$I(d) = I(0)e^{-\mu d} \tag{2.4}$$

The absorption in different media is given in table 2.2 Due to the absorption, classical ray-based ultrasound imaging methods are not capable of mapping the absolute reflection coefficients, hence the images have to be interpreted qualitatively. The absorption reduces the image quality, which makes remote objects and weak reflectors invisible (Carstensen, 1998).

There exist different ultrasound systems. For instance, common handheld devices that are widely used for abdominal ultrasound imaging are unlikely to be adopted for breast

screening. They are operator dependent and the aperture does not allow whole breast screening, either. Automated breast ultrasound systems with a fixed geometry reduce the operator dependence and increase the field of view (Duric and Littrup, 2018). The breast is immersed in a water bath surrounded by transmitters and receivers and scanned by an automated mechanism. The water is used to couple the transducers with the skin. These scanners can potentially make reproducible high-quality volumetric images of the breast (Ozmen, 2014).

2.3.2. USCT

One such automated system is the Ultrasound Computed Tomography System (USCT), developed at the Karlsruhe Institute of Technology. The device has a semi-ellipsoidal 3D aperture with a diameter of 26 cm and a height of 16 cm. Each emitter generates an approximately spherical wavefront at 2.5 MHz. The spectral power is reduced by −6 dB at a bandwidth of 1.5 MHz. The current design has 628 emitters and 1413 receivers, sampling the data with a rate of 20 MHz. Temperature sensors allow tracking the temperature distribution within the water basin. The system is depicted in figure 2.1. (Ruiter et al., 2017)

2.4. Ultrasound imaging algorithms

Conventional ultrasound reconstruction techniques are based on a simple wave propagation model derived from a high-frequency approximation. A higher frequency has a shorter wavelength, which allows to produce images with a better resolution but also leads to an increased absorption of the waves, so operating at higher frequencies comes at the cost of lower signal-to-noise ratio (Roy et al., 2016). In ultrasound medical imaging, the central frequency of the input pulse is typically chosen between 0.5 and 15 MHz. These frequencies have a wavelength that is short enough to detect the structures in the human body (Sandhu et al., 2015; Roy et al., 2016). The following algorithms require first an initial forward model which describes well the underlying physical system and second measurements of good quality. The accuracy of the forward model, the fidelity of the measurements and the choice of the inverse method have direct influence on the quality of the estimated model (Hormati et al., 2010).

2.4.1. Obtaining a velocity model: Tomography

The following algorithms are capable to reconstruct an approximate distribution of the velocity in the measured area. They apply iterative schemes that require a starting velocity model $m_1 :\ m_2 = m_1 + \delta m$. The model update δm yields an improved velocity model m_2. The algorithms minimize the misfit $\vec{u}^{obs} - \vec{u}^{mod}$ between the observed seismograms u^{obs} and the modeled seismograms u^{mod} in the least-squares sense, which has the physical interpretation of energy E. In this case the data $\vec{u}$ describe the measured pressure $p(t, \vec{x}_r)$ at the receiver positions $\vec{x}_r$.

$$E = (\vec{u}^{obs} - \vec{u}^{mod})(\vec{u}^{obs} - \vec{u}^{mod})^T \tag{2.5}$$

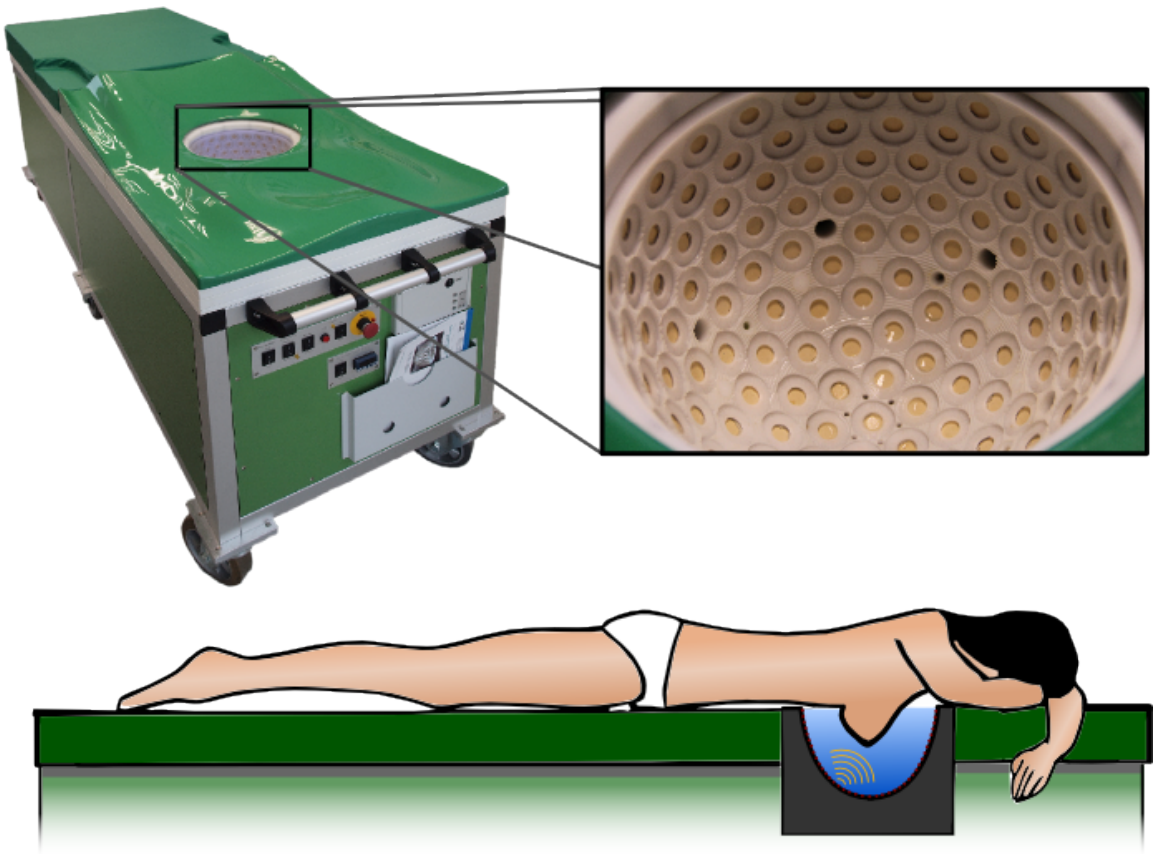

Figure 2.1.: Sketch of the USCT system. A woman immerses the breast in the water bath. The surrounding ultrasound imaging system scans the breast and calculates the origin of the reflections. Source: Institut für Prozessdatenverarbeitung und Elektronik, KIT (2018)

Bent-ray reconstruction

The bent-ray reconstruction employs the principles of geometrical acoustics to estimate the sound speed distribution $v(\vec{x})$. It is based on the fact that if the medium behaves isotropic, acoustic energy travels along the lines perpendicular to the equal-phase wavefronts which is a valid assumption at high frequencies. Then, the ultrasound ray paths can be found using Fermat's principle (Hormati et al., 2010) and the resulting Snell's law. Then, the inverse problem consists of reconstructing the sound speed distribution $v(\vec{x})$ from the traveltime data estimated from the recorded waveforms. The modeled data $\vec{u}^{mod}$ in equation 2.5 can be calculated with

$$\vec{u}^{mod} = G(m)\ \vec{m} \tag{2.6}$$

where $\vec{m}$ is the unknown slowness distribution model $1/v(\vec{x})$ of size N, $G(m)$ is the ray-length matrix of size M x N that describes the propagation path and $\vec{u}^{mod}$ is the data vector of size M. An iterative approach then minimizes the misfit 2.5. One possibility is the Gauss-Newton method where one iteratively finds the acoustic paths for the current model estimate and solves the resulting linear system for an updated model (Hormati et al., 2010). This approach consists of iteratively performing the following steps:

1. Find the ray paths for the current velocity estimate and build the corresponding ray-length matrix
2. Solve the resulting linear system of equations 2.5 and 2.6 and update the slowness distribution

Backpropagation, Born inversion and contrast source inversion

Backpropagation, Born inversion and contrast source inversion use a decomposition of the incident wavefield $p^{inc}(\vec{x}, t)$ generated by the primary source and a scattered field $p^{sct}(\vec{x}, t)$ generated by the reflections:

$$p(\vec{x}, t) = p^{inc}(\vec{x}, t) + p^{sct}(\vec{x}, t) \tag{2.7}$$

It can be shown that the Fourier transform of the scattered field $p^{sct}(\vec{x}, t)$ equals

$$\begin{aligned} \hat{p}^{sct}(\vec{x}) &= \omega^2 \int_{\vec{x}' \in D} \hat{G}(\vec{x} - \vec{x}')\ \hat{p}(\vec{x}')\ \xi(\vec{x}') dV(x') \\ \xi(\vec{x}') &= \frac{1}{v^2(\vec{x}')} - \frac{1}{v_0^2} \end{aligned} \tag{2.8}$$

where $\hat{G}(\vec{x} - \vec{x}')$ is the Green's function describing the impulse response of the background medium and where the contrast function $\xi(\vec{x}')$ describes the variations in the speed of sound of the constant speed c_0 of the background medium due to the presence of objects in the spatial domain D (Ozmen et al., 2015). The equations 2.7 and 2.8 can be linearized by replacing the unknown field $\hat{p}(\vec{x})$ by the known incident field $\hat{p}^{inc}(\vec{x})$, which is in literature referred to as the Born approximation (not to be confused with the Born

inversion) (Ozmen, 2014). Then, backpropagation, Born inversion and contrast source inversion use different approaches to minimize the misfit between the observed and the synthetic seismograms, usually in the least-squares sense (see equation 2.5). Backpropagation has only one iteration, Born inversion and contrast source inversion are iterative algorithms. (Ozmen, 2014; Ozmen et al., 2015; Abubakar et al., 2009; Han et al., 2014).

Comparison

Ozmen et al. (2015) test and compare the techniques on a synthetic data set including noise, representing a 2-D tomographic scan of a breast with a 4-cm-diameter tumor using a circular array with 157 transducers and a center frequency of 110 kHz. The relatively low frequency has computational advantages and also enhances the differences between the results of the different algorithms, facilitating a comparison. This way they demonstrate that backpropagation produces blurry images, mainly showing the water-breast interface. The Born inversion method yields a correct localization of the breast and can reconstruct most of the internal structures, albeit with wrong amplitudes. The authors emphasize that the inversion is unstable, and for real data sets it would not be clear how to choose the stopping criterion of the algorithm. Only with contrast-source inversion, the breast, the tumor, and almost all internal structures are identified with (nearly) correct amplitudes.

Unfortunately, backpropagation or contrast-source inversion are not applied in a field application yet, because they are computationally very expensive.

Full-waveform inversion (FWI)

Full-waveform inversion consists of the following steps:

1. Collect the seismograms $\vec{u}^{obs}$ and define a starting model m_1
2. Calculate how the wavefield would spread in the starting model (forward propagation)
3. Form the residuals $\delta\vec{u} = \vec{u}^{obs} - \vec{u}^{mod}$ between the observed seismograms $\vec{u}^{obs}$ and the modeled data $\vec{u}^{mod}$
4. Calculate the residual wavefield (backward propagation)
5. A cross-correlation between the forward wavefield and the residual wavefield leads to an unscaled model update
6. Calculate the step-length of the model update
7. A combination of the unscaled model update with the estimated step-length leads to a scaled model update.
8. Iterate until the misfit E is reduced to a threshold

This iteration leads to a locally optimal model m, which minimizes the residual energy E (equation 2.5).

2.4.2. Migration with synthetic aperture focusing technique

The synthetic aperture focusing technique creates a map with the reflectors. The procedure of creating a map of reflectors is called migration. The synthetic aperture focusing technique requires a velocity model in order to calculate the traveltime $T_{s,r}^{cal}(\vec{x})$ from the source s to a pixel at position $\vec{x}$ to the receiver r. This procedure is repeated for all pixels and saved. Then, for the image point at position $\vec{x}$, the measured pressure $p_{s,r}^{sct}$ at the calculated traveltime $T_{s,r}^{cal}(\vec{x})$ is read from the seismograms. Repeating this procedure for all sources and receivers and summing the results leads to constructive and destructive interference of the corresponding measured pressures, yielding the value of the image point. The procedure is applied for all image points, which produces the map of reflectors (Scheben, 2012). So the contrast function X^{SAFT} is calculated with

$$X^{SAFT}(\vec{x}) = \sum_{s,r} p_{s,r}^{sct}(T_{s,r}^{cal}(\vec{x})). \tag{2.9}$$

The maximum phase shift caused by the variations in the speed of sound should be smaller than π, otherwise the constructive/destructive interference principle fails (Ozmen, 2014). The synthetic aperture focusing technique assumes single scattering for the reconstruction of images from the measured data. Multiple reflections cause artifacts in the reconstruction (Hardt et al., 2012).

The advantage of ray-based imaging algorithms like the synthetic aperture focusing technique is their low computational cost, which allows real-time applications. The price is the neglectance of many wave phenomena such as refraction and multiple scattering. They all play a role in breast ultrasound and therefore should be taken into account during imaging. Taking account of these phenomena possibly improves the reconstruction of structures as complex as the female breast.
Ozmen et al. (2015) also compare the synthetic aperture focusing technique with the other tomography algorithms. The image obtained with the synthetic aperture focusing technique is similar to the result of backpropagation, a blurry image, mainly showing the water-breast interface. However, this technique additionally reproduces some internal structures of the breast.

3. Reverse-time migration

Reverse-time migration has been initiated in Geophysics in the early 1980's (Zhou et al., 2018). The method uses the solution of the full wave-equation 2.1 to create an image with the reflectors. This allows to take into account all wave phenomena, which is the main advantage over ray-based methods like the synthetic aperture focusing technique, the accompanying increased computational effort is its main disadvantage. A possible solution method of the wave-equation is a finite-difference approach, which is described in section 3.2. To the author's best knowledge, reverse-time migration is not recognized in ultrasound medical imaging yet. Roy et al. (2016) have done the first study of this method for ultrasound breast screening, but besides their examinations no other research on reverse-time migration in this research area is published so far.
The principle of reverse-time migration is based on an idea by Claerbout (1981), who finds that "reflectors exist at points in the ground where the first-arrival downward wave is coincident with an upgoing wave in time". The implementation of this conception works as follows: An acoustic wave may be generated by a source at time t_0. An object in the subsurface reflects the downgoing wavefield at time t_1. Then the reflected, upcoming wavefield is registered at a receiver at time t_2. Let T^{mes} annotate the measured traveltime between shot and receiver, $t_2 - t_0$. So the time the wave travels from source to reflector equals $T_{down} = t_1 - t_0$ and the time from reflector to receiver amounts $T_{up} = T^{mes} - T_{down}$. This means that the downgoing wavefield and the upcoming wavefield at the reversed time $T - T_{up}$ overlap locally at the reflector at time t_1.
This principle leads to the basic idea of reverse-time migrations. It requires the availability of a velocity and density model of the subsurface in order to compute the simulated wavefields. At first, the wavefield that spreads from the source at time t_0 is modeled for any time step $t_i < T$ by numerically solving the equations 2.1. Then, a theoretic backward propagating wavefield is computed, starting at time t_2 at the receivers with the boundary condition given by the measured seismic data. Afterwards the forward wavefield at time t_i is pixelwise multiplied with the backward-propagated wavefield at time $T - t_i$ and finally summed over all time steps and shots. Mathematically, this equals their zero-lag cross correlation. With the source s and receiver r, the forward propagating wave from source s p_s^{forw} and the backward propagating wave $p_{s,r}^{back}$, the obtained image is computed with

$$X^{RTM}(\vec{x}) = \sum_{s,r,t} p_s^{forw}(\vec{x}, t) p_{s,r}^{back}(\vec{x}, T^{mes} - t) \tag{3.1}$$

The results will interfere constructively at the reflectors, and this method can be used to migrate the measurements to receive a map of reflectors.

All in all, the algorithm consists of three steps and two additional steps for data pre- and post-processing:

1. Find a velocity model $v(\vec{x})$ of the subsurface
2. Data pre-processing
3. Forward propagation of the source wavefield
4. Backward propagation of the receiver wavefield
5. Applying an imaging condition to construct the image
6. Image post-processing

The forward wavefield is saved at every time step so the multiplication with the backward wavefield can be implemented while computing the latter.

3.1. Data pre-processing

The reverse-time migration produces image artifacts, a problem that is discussed in chapter 3.3. Removing the direct wave will significantly reduce these imaging artifacts. Seismological and seismic research introduced different possibilities to pick and remove the direct wave from seismic data (for example, see Ross and Ben-Zion (2014) or Lee and Shin (2011)). The author develops a simpler attempt. A model with constant impedance Z and the original velocities is created by setting the density of the model to $\rho_{hom.Z} = Z_{const}v$. According to equations 2.2 and 2.3, this model does not cause any reflections, hence only the direct waves are recorded by the receivers. These are subtracted from the seismograms of the original model, which now contains only the reflected waves. Finally, the backpropagation is started with the modified seismograms. The results of this approach are satisfactory (see section 4.6) and the advanced techniques are not applied here.

3.2. Wavefield extrapolation

After preprocessing the seismic data, the forward- and backward-propagated wavefields are modeled numerically. There exist one-way and two-way wavefield extrapolation methods. One-way methods are typically derived by the factorization of some form of the wave equation. They assume mild lateral variations and an approximate propagation in the preferred direction. The advantages of one-way approaches are the relative ease of implementation and computational efficiency (Shin, 2003). However, the assumptions hardly apply in the female breast. Consequently, a two-way extrapolation that simulates the full wave propagation using the finite-difference method is applied. For this purpose the wave equation 2.1 has to be discretized in time and space on a grid. The particle velocity $\vec{v}(\vec{x})$ and the medium density $\rho(\vec{x})$ are defined at discrete Cartesian coordinates $\vec{x} = (x, y, z) = (i, j, l)dh$ and discrete times $t = n\ dt$. The term dh denotes the spatial distance between two adjacent grid points and dt the difference between two successive time

steps. Then the derivative of a function f with respect to a variable x can be approximated by the forward and backward operators (Köhn, 2011):

$$D_x^+ f = \frac{f[i+1] - f[i]}{dh}$$
$$D_x^- f = \frac{f[i] - f[i-1]}{dh}$$

This is the first-order approximation of the derivative operator. The first derivate can be calculated more precisely with operators of higher order which make use of a larger number of image points. Other discrete operators like the second derivate can be constructed similarly.
In this way equation 2.1 can be solved numerically. However, the discrete approximation is not perfectly precise. The spatial grid between two gridpoints affects the result. There have been many studies on this topic (for example Köhn et al. (2012); Courant et al. (1928); Holberg (1987); Moss et al. (2002); Haixia et al. (2014)). They prove that a numerically calculated wavefield is dispersive. Accordingly, the numerical artifacts are called grid dispersion. The artifacts can be avoided sufficiently well if the spatial grid spacing dh satisfies $dh < v_{min}/n\ f_{max}$, where f_{max} denotes the maximum frequency of the signal, v_{min} denotes the minimum velocity in the model and n is the number of grid points per wavelength.
The temporal discretization has to ensure that the time step is smaller than the time the wave needs to travel between two grid points. This means that dt has to satisfy $dt < dh/\sqrt{2}v_{max}$ (Köhn, 2011).
The waves are damped when they reach the border of the water bath. A numeric possibility to damp waves at boundaries are perfectly matched layers. This can, for instance, be achieved by a coordinate stretch of the wave equations in the frequency domain (Komatitsch and Martin, 2007).

3.3. The imaging condition

The forward-propagated wavefields at time t and the backward-propagated wavefields at time $T - t$ are multiplied and summed over all time steps and sources, which equals the cross-correlation of the two wavefields (Liu et al., 2011). Consequently, this imaging condition is referred to as cross-correlation imaging condition (Liu et al., 2011; Jones, 2014). Unfortunately, this imaging condition produces some unwanted side effects. Figure 3.1 illustrates how the direct waves correlate along the raypath from the source to the receiver, but they do not correlate at the reflector. Therefore they do not contribute for mapping the reflectors, but only produce image artifacts. Hence, removing the direct waves from the seismograms should improve the image quality.
Furthermore, in a two-way wavefield extrapolation, the reflected waves and the time-reversed reflected waves always travel at the same time and in the same space and cause severe artifacts (Jiang et al., 2017). In figure 3.1, this artifact is illustrated green. It can be seen that this artifact spreads everywhere on the path from the source to the reflector to the receiver. This type of noise is unique to reverse-time migrations: One-way

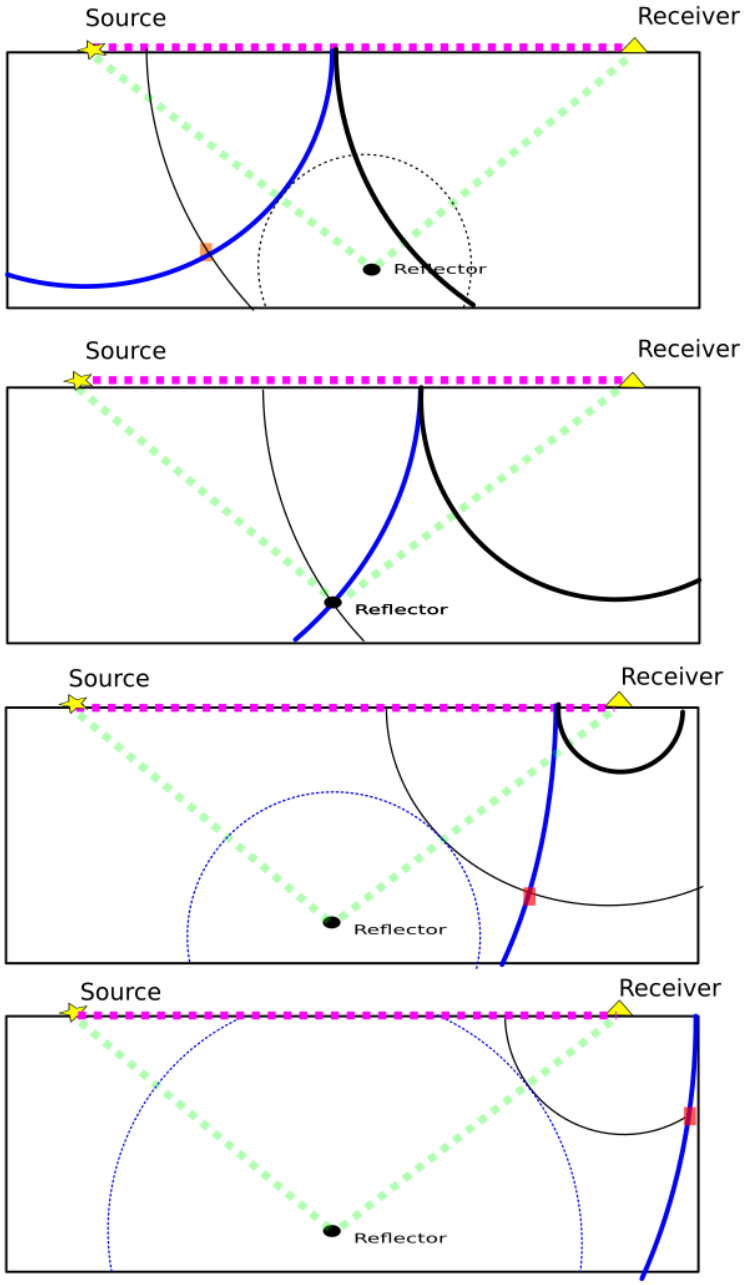

Figure 3.1.: Cross-correlation of the forward (blue) and time-reversed backward (black) propagated wavefield for a simple small reflector in a homogeneous half space at three different timesteps. The direct waves (thick) correlate on the straight path from source to receiver (pink line). In a two-way wavefield extrapolation, the reflected waves (dotted) coincide at every point along the path from source to reflector to receiver (green line). The thin solid line is the (time-reversed) transmitted wave.

wave equation based migrations using the same cross-correlation imaging condition do not produce this noise (Liu et al., 2011).
The direct and the time-reversed transmitted waves coincide at different points, which is marked orange and red in figure 3.1. Since these two waves travel in different directions, their overlap appears only very short at the same place, so this kind of imaging artifact distributes in limited space (Jones, 2014). Removing the direct wave from the seismogram will remove the orange artifact produced by the upgoing transmitted wave. The red artifacts will not be removed, since they are an artifact produced by the downgoing transmitted wave whichs correlates with the reversed reflected wave.
Other typical artifacts of the cross-correlation imaging condition are lateral amplitude terminations on strong vertical boundaries (localized edge effects) and laterally mispositioned double bounce arrivals (Jones, 2014). Liu et al. (2011) point out that the cross-correlation imaging condition produces large-amplitude noise that contaminates the image near sharp interfaces. Sometimes these noises can even completely mask the signals. Although those noises appear to have much lower frequency than the signals, simple band-pass filtering fails to completely remove their imprint (Liu et al., 2011).

Various authors have introduced alternative, more complex imaging conditions that are capable to reduce the number of artifacts. Sava and Fomel (2003) uses a time shift before computing the cross-correlation of the wavefields to calculate angle gathers, the corresponding imaging conditions are known as extended imaging condition. Liu et al. (2011) calculate the Hilbert transform of the wavefield to determine the direction of the propagating wave and use this information to add additional restrictions to the imaging.

3.4. Postprocessing

An effective way to reduce the artifacts produced by the cross-correlation imaging condition is post-processing the images.

3.4.1. Laplacian image filter

The most common image filter in literature is the Laplacian filter. The two-dimensional operator is defined as

$$\Delta f(x,y) = (\frac{\partial^2}{\partial x^2} + \frac{\partial^2}{\partial y^2}) f(x,y). \tag{3.2}$$

In the discrete case of an image, this operator assigns to an image point the summation of the eight pixels i that directly lie up, down, left, right and diagonal. From this summation the value of the centered pixel is substracted eight times. The operator is illustrated in table 3.1. The filter is applied on example image values in table 3.2. It demonstrates that the Laplacian filter sharpens lines and edges and removes fields of constant value.

3.4.2. Laguerre-Gauss filter

Guillermo and Sierra-Sosa (2016) propose the usage of a technique based on a spiral phase filter ranging from 0 to 2π, and a toroidal amplitude bandpass filter, known as Laguerre-

Table 3.1.: The Laplacian image operator: Pixelwise multiplication factors of the original image.

0	0	0	0	0
0	1	1	1	0
0	1	-8	1	0
0	1	1	1	0
0	0	0	0	0

Table 3.2.: The Laplacian operator: comparison of original picture and filtered image

0	0	0	0	0	0	0	0
0	0	10	10	10	10	0	0
0	0	10	10	10	10	0	0
0	0	10	10	10	10	0	0
0	0	10	10	10	10	0	0
0	0	0	0	0	0	0	0

0	10	20	30	30	20	10	0
0	20	-50	-30	-30	-50	20	0
0	30	-30	0	0	-30	30	0
0	30	-30	0	0	-30	30	0
0	20	-50	-30	-30	-50	20	0
0	10	20	30	30	20	10	0

Gauss transform. They show that this filter enhances the edges without resolution loss, and the low-frequency noise is removed, so the reflective events are more defined. Let $I(x, y)$ be the original intensity distribution from an image and $\hat{I}(k_x, k_y)$ its Fourier transform, where k_x, k_y denote the wave numbers. In the wavenumber domain, the image is multiplied with the factor

$$LG(k_x, k_y) = \alpha e^{-(\frac{\alpha^2}{\omega^2})} e^{i\varphi}, \tag{3.3}$$

where $\alpha = \sqrt{k_x^2 + k_y^2}$ and $\varphi = \arctan(k_y/k_x)$ are the polar coordinates in the wavenumber domain. The bandwidth parameter ω controls the width of the bandpass filter (W. Wang et al., 2006). As it can be set arbitrarily, the bandpass filter is chosen in way the visual result is best. Then the filtered image $\tilde{I}(x, y)$ is calculated by transforming the result back to the spatial domain. So the filtered image equals

$$\tilde{I} = \int \int_{-\infty}^{\infty} LG(k_x, k_y)\hat{I}(k_x, k_y)e^{2\pi i(k_x x + k_y y)} dk_x dk_y \tag{3.4}$$

Finally, only the real part of the image is considered.
In the numerical experiments in section 4, both filters are applied and their result is compared.

4. Experimental results

In the following section, numeric experiments aim to further estimate the capabilities of the proposed reverse-time migration in medical ultrasound imaging. Furthermore, the prerequisites to reasonably apply the algorithm are described. The goal of the experiments is to bring reverse-time migration closer towards a field application. In order to achieve this goal, the algorithm is applied on a two-dimensional cross section through a female breast model, performing a migration of synthetic seismograms. The reduction of the model to two instead of three dimensions reduces the computational cost.

4.1. The measurement setup

The reference model (figure 4.1 and 4.2) describes a cross section through an acoustic female breast phantom immersed in water, generated by Lou et al. (2017) for use in USCT and others. The phantom depicts the skin layer with a thickness of approximately 5 mm with a sound velocity of 1650 m/s and a density of 1150 kg/m^3, vascular structures, and the volumetric distribution of different tissue types in the breast (1470 − 1515 m/s, 937 − 1040 kg/m^3. A tumor with $v = 1530$ m/s and $\rho = 1020$ kg/m^3 is located at 0.075 m in x-direction and 0.14 m in y-direction (definition of x- and y-direction in figure 4.1). Image 4.3 shows the reflection coefficients of the model for plane waves with orthogonal angle of incidence. The coefficients are calculated using equation 2.3, with Z_1 being the impedance of the left-neighboring pixel of the corresponding calculated pixel with the impedance Z_2. The model has a size of 1200x1200 pixels, each corresponding to a spatial resolution of 0.2 mm. The velocity in the model ranges from 1470 m/s to 1650 m/s. The density varies from 970 kg/m^3 to 1150 kg/m^3. The measurement setup consists of a set of 256 receivers and 16 ultrasound transducers with an operating frequency of 500 kHz symmetrically arranged in a circular array around the breast. A higher frequency requires a finer grid spacing in the model, which means higher computational cost. Due to that, a compromise is necessary between the simulated frequency in the following experiments and accordance with real measurement setups. The model and the transducer positions are illustrated in figure 4.1, a list with the precise source positions is attached in appendix A.2.
The absorbing boundary is implemented with perfectly matched layers (described in section 3.2) with a width of 96 pixels that damp waves with a velocity of 1500 m/s and a frequency of 500 kHz. The reason for the extension to 96 pixels instead of 10-20 pixels, which would be sufficient for monofrequent wavefields, lies within the experiments described in chapter 4.7.3. White Gaussian noise is added to the modeled seismograms, which has a different frequency spectrum than the waves. Hence the noise might be reflected at the image borders and cause artifacts. There exist many techniques for noise

filtering (for example Kuan et al. (1985); Alsdorf (1997) or Djarfour et al. (2014)), which are not applied here.

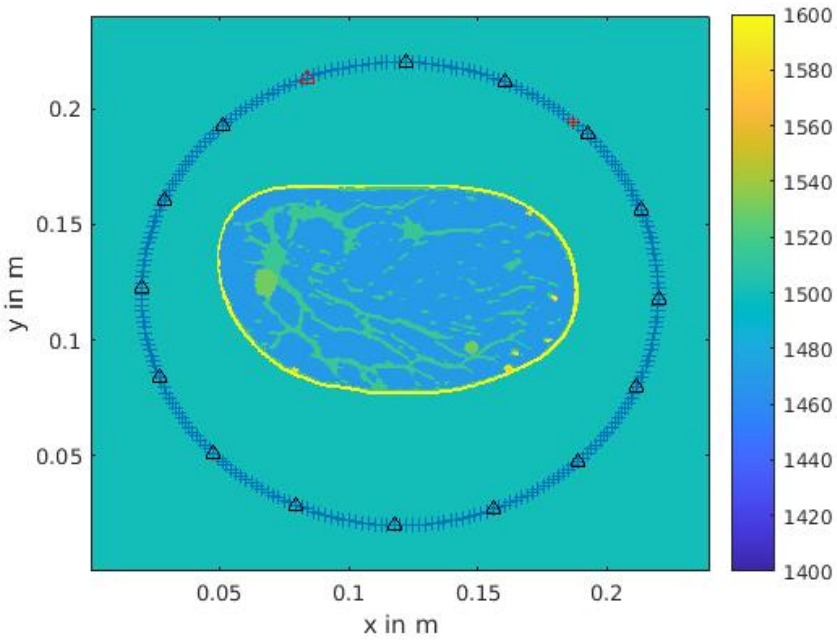

Figure 4.1.: The velocity of the reference model, sources (triangles) and receivers ('+'). Velocity in m/s

.

4.2. Wavefield extrapolation

The experiments use an finite-difference order of eight, which means that the dispersion error is less than 0.1 %. The time interval for the numeric wavefield simulation equals the sampling interval of the seismograms and amounts to $2\ 10^{-8}$ s. A snapshot of a wavefield at four different time steps can be seen in figure 4.4.

Besides the propagation of the transmitted wave, the snapshot also shows a lot of reflections that move in all directions. The complexity of the wavefield justifies the usage of a two-way propagator, since one-way propagators assume an approximate propagation in a preferred direction (see section 3.2), which is obviously not the case. A look at the seismograms, which is, for instance, illustrated in section 4.6, figure 4.10, shows that the traveltime of the wave through the breast amounts less than a millisecond.

4.3. Quality estimators

Besides a visual characterization of the results of the following experiments, an automated quantitative specification helps to evaluate the impact of changing influencing factors. The sharpness of the images and the amount of their artifacts cover the aspects of image

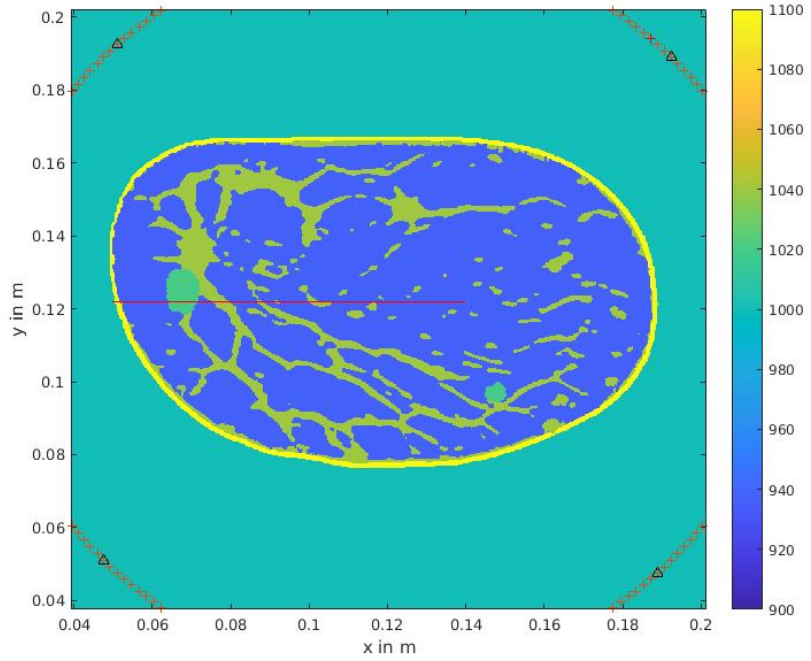

Figure 4.2.: The density of the reference model. The red line describes the profile used for the measurement of the line width. Density in kg/m^3.

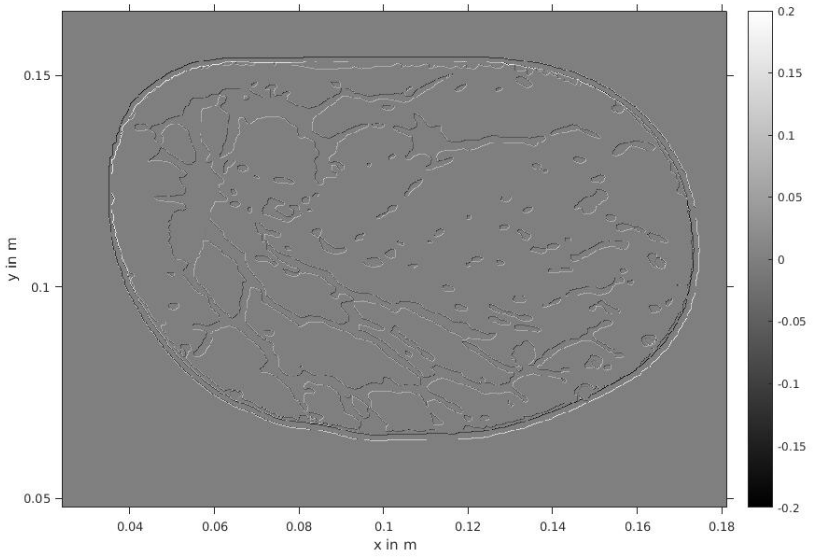

Figure 4.3.: The theoretical reflectivity coefficients of the breast model for waves traveling from the left to the right side.

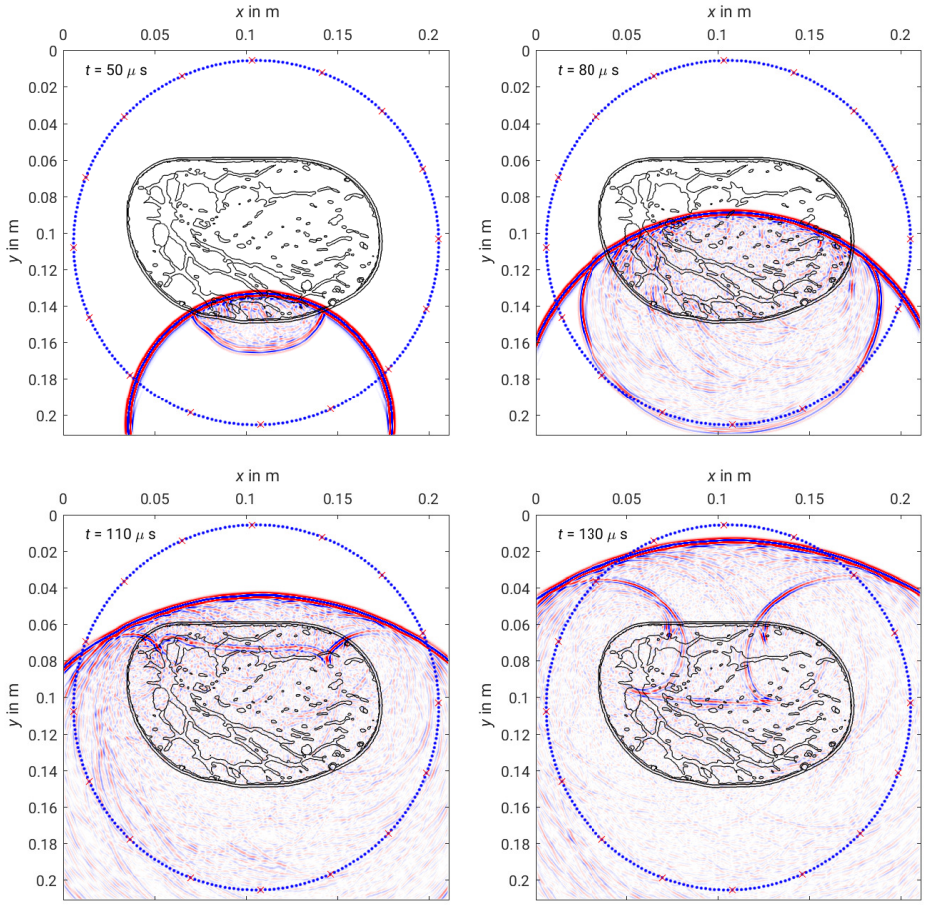

Figure 4.4.: Snapshots of the calculated wavefield for one source at four different timesteps. By Fabian Kühn (see acknowledgements).

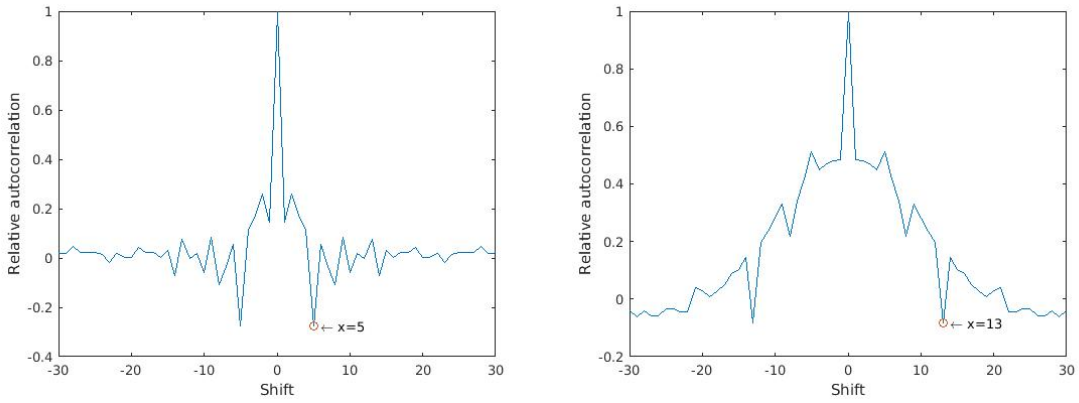

(b)

Figure 4.5.: Auto-correlation functions of the smoothed Laplacian reflectivity image at line 528 from pixels 100 to 900. The image is smoothed by two-dimensional convolution with a constant matrix of size five (left) and thirteen (right). The minimum values of the function occur at the corresponding shifts.

analysis sufficiently. The author developed two measures to obtain such an estimation of these aspects.

- Sharpness:
  The Laplacian images are evaluated using the auto-correlation of the image. As a sharp edge of the image results in positive values inside the form and negative values on the neighboring pixels outside (compare table 3.2), the auto-correlation with a one pixel shift is negative. Consequently the lag to the next local minimum of the auto correlation is a good measure of the sharpness of the image and might be interpreted as the width of lines and edges, hence it is referred to as line width in this study. It assumes that the measured line lies orthogonal to the profile of the correlation estimation.
  In order to verify this consideration, the estimator is applied on the reflectivity image 4.3 and on smoothed versions of it. The smoothing procedure is a two-dimensional convolution with a constant square with a width of five and thirteen pixels. In order to satisfy the orthogonality condition, only the pixels in the mid of the y-direction with an x-range from 100 to 900 are used, illustrated as a red dotted line in figure 4.2. The auto-correlation plots can be seen in figure 4.5. Indeed, the measured line width equals the expected values of one, five and thirteen pixels. These results demonstrate that this estimator measures the line width properly. The line width cannot identify wrong reflections (artifacts).

- In order to quantitatively compare the number of artifacts, another estimator is introduced: Firstly, every pixel of the Laplacian filtered image with an imaging energy above a threshold is defined to be a reflector. The estimator is applied on the Laplacian filtered image since this filter removes fields of constant values, which allows to distinct between the interior of a structure and its interface (the reflector)

to the surrounding medium.
Reverse-time migration maps imaging energy due to the cross-correlation imaging condition, and the imaging energy does not agree with the reflection coefficient. The amount of imaging energy required to define a pixel to be a reflector is arbitrary. The reflectors of the image are compared with the theoretical reflectivity model and categorized as a true positive if the reverse-time migration denotes it as a reflector correctly. It is defined as a false positive, if the reverse-time migration selects it to be a reflector but there is none in the model at this position. The number of false positives is a measure to describe the number of artifacts, because this measure describes how many reflectors the image contains where none is.
False negatives are pixels that the reverse-time migration fails to recognize as being a reflector. True negatives are pixels that are no reflectors, neither in the reverse-time migration result nor in the model. The sum of true positives and false negatives is a constant and equals the total number of reflectors in the image.
The amount of total and local imaging energy changes in the different experiments, which distorts the results. Normalizing the results by fixing the number of true positives as a constant by varying the threshold of imaging energy required for a reflector solves this problem.

4.4. The result and its improvement with image filters

At first the reverse-time migration code is applied on the data without any pre- or post-processing. The result can be seen in figure 4.6. Structures within the breast can be seen clearly, but there occur many artifacts. Their origin lies within the imaging condition (see section 3.3). There is a dark blur covering some areas. Gradients in areas where the model is constant can be found and lines stretching tangential to the water-breast interface disturb the image considerably. Some small structures are smeared.

Laplacian filter

The Laplacian filter (chapter 3.4.1) enhances lines and edges and removes fields of constant values. Figure 4.7 shows the result of the application of the filter on image 4.6. Now the artifacts vanish almost completely and even small details are mapped sharply. For example, the skin is delineated both from the water and from the soft tissue. The measured line width amounts to two pixels. All in all the image reaches almost perfect sharpness with possible improvements of the contrast.

Laguerre-Gauss filter

Applying the Laguerre-Gauss filter (chapter 3.4) on image 4.6 yields the image in figure 4.8. The filter leads to a smoother background and an enhanced depiction of contours. However, a visual comparison with the results of the Laplacian filter reveals that the latter

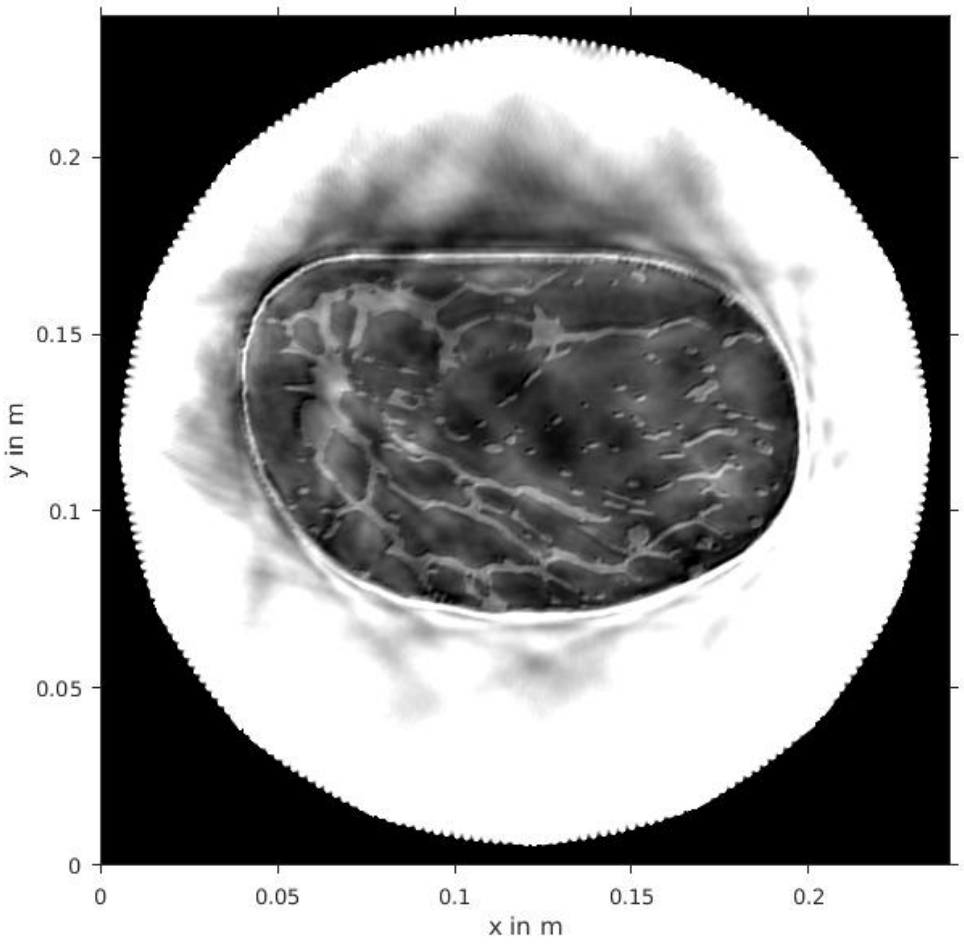

Figure 4.6.: Result of the reverse-time migration imaging without any pre- or postprocessing with a center frequency of 500 kHz.

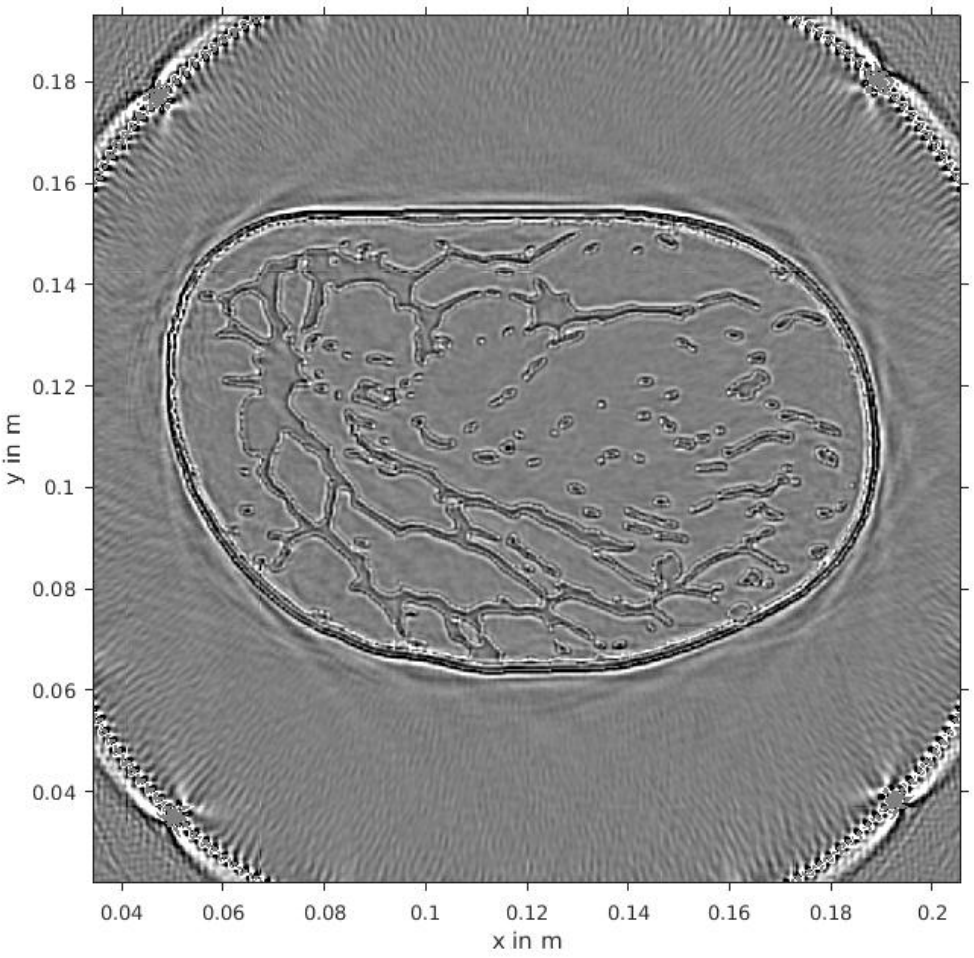

Figure 4.7.: Laplacian-filtered result without pre-processing and a center frequency of 500 kHz.

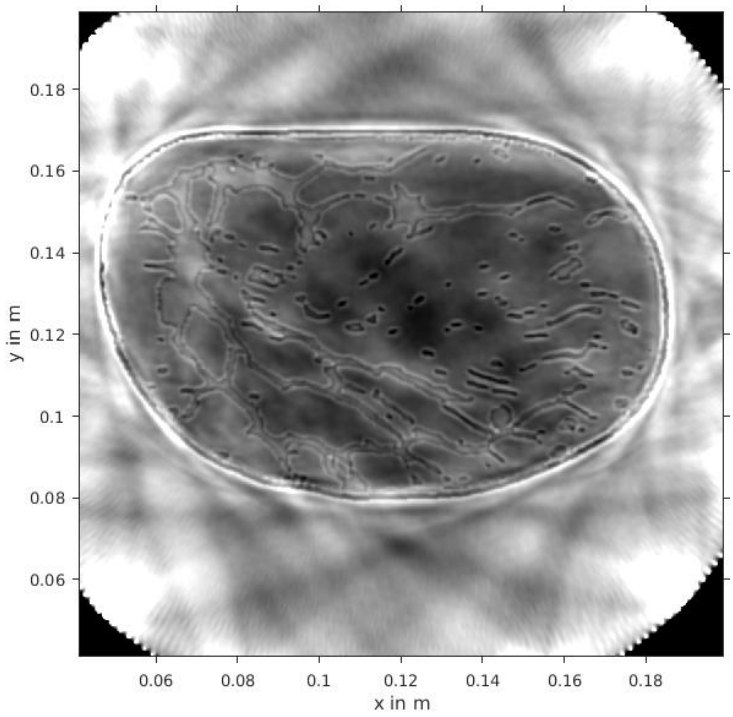

Figure 4.8.: Image 4.6 after application of the Laguerre Gaussian image filter with a bandwidth ω of 2 cm.

is superior in depicting the lines and edges. In addition, image artifacts are eliminated better with the Laplacian filter.

4.5. Comparison to the synthetic aperture focusing technique

The synthetic aperture focusing technique, in Geophysics also known as Kirchhoff migration, is a ray-based reconstruction technique and therefore neglecting many wave phenomena. In order to determine if the advantages of reverse-time migration, such as the solution of the full wave-equation, improve the image quality, a direct comparison is necessary. Reconstructing the breast with the synthetic aperture focusing technique yields figure 4.9. The result is a good reconstruction of big structures. The synthetic aperture focusing technique fails in imaging the small structures which can be found, for instance, from 13 to 16 cm in x-direction. The image suffers from artifacts that cause an inhomogeneous background, smearing small structures. A comparison between the results of reverse-time migration and synthetic aperture focusing technique demonstrates that both algorithms are capable to localize tissue changes as they occur in the female breast. However, if the size of the structures becomes smaller than about half a centimeter, the reconstruction with the synthetic aperture focusing technique looses contrast and sharpness, while reverse-time migration is still capable to map these structures. The measured line width fits this observation. For the synthetic aperture focusing technique it amounts to six pixels, so reverse-time migration is three times sharper.

4.6. Direct wave removal

The following section aims to reduce the image artifacts by removing the direct wave with the procedure described in chapter 3.1. Figure 4.10 illustrates the result. The red line is the plot of the blue seismogram after reduction of the calculated direct wave. The seismic data belong to the red shot and the red receiver in figure 4.1. Obviously, there remain some residuals of the direct wave at time 0.074 s. However, the amplitude of the residual is much smaller than thae original and of the same order as the amplitudes of the reflections that arrive after approximately 0.09 s. With these seismograms, the reverse-time migration produces image 4.12. In the case of this source/receiver arrangement, there is a time lag between the arrival of the direct wave after approximately 0.75 ms and the arrival of the reflected waves after 0.9 ms. Consequently, an alternative and possibly more effective technique to remove the direct wave would be to mute any signal before 0.83 ms. Figure 4.11 shows the seismogram which belongs to the same source and the receiver that lies on the other side of the array ring and therefore also on the other side of the breast. In this case, it is not possible to remove the direct wave by muting a time-window without affecting the reflected waves, because it is not possible to distinguish between the arrival of the direct wave and the arrival of the reflected waves. This problem is the reason why the technique of time-windowing is not applied in this study. A comparison with the original result in figure 4.6 reveals that removing the direct waves from the seismic data clearly enhances the image contrast. The water-breast interface can be localized more precisely. Besides, the background's improved homogeneity makes it easier to concentrate on the details.

Figure 4.13 shows the image after applying the Laplacian filter. Compared to the original result (figure 4.7) the contrast is enhanced, too.

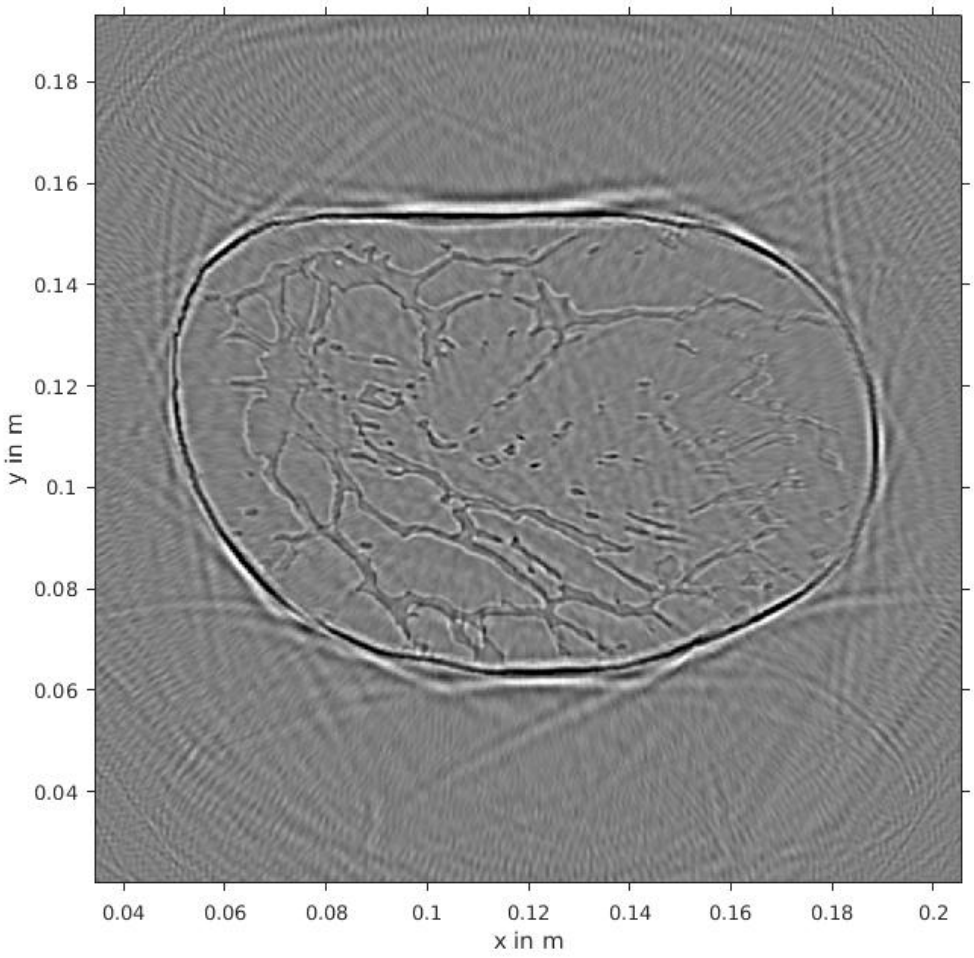

Figure 4.9.: Breast reconstruction with SAFT using the reference model with a center frequency of the sources of 500 kHz. By Torsten Hopp (see acknowledgements).

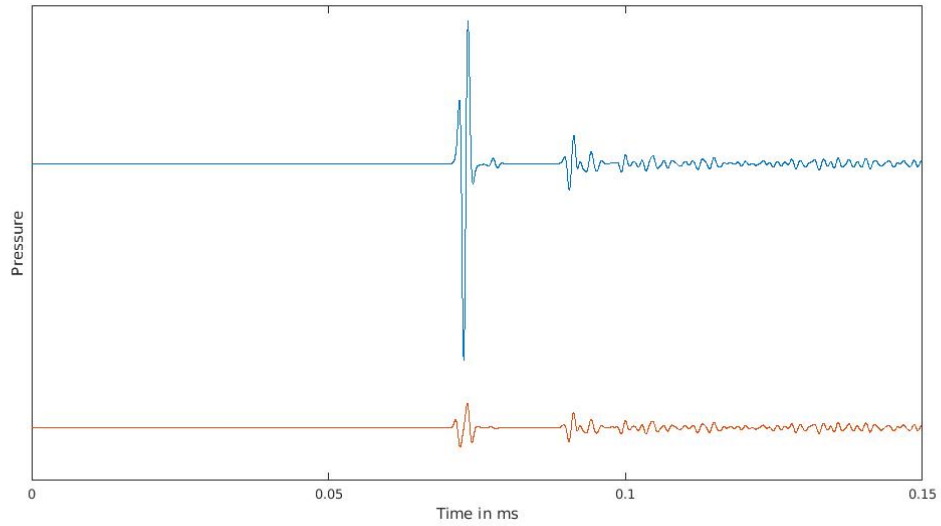

Figure 4.10.: One original seismogram (blue) and with an attenuated direct wave (orange-red)

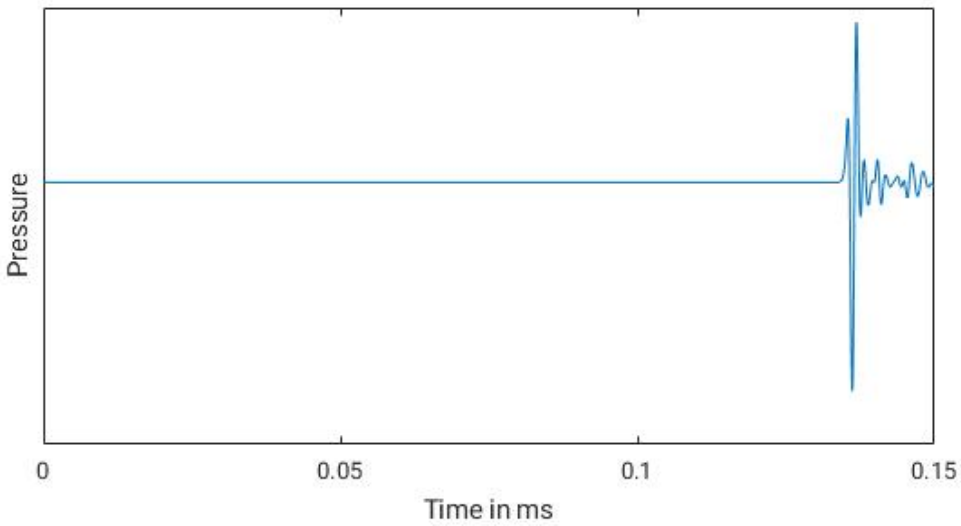

Figure 4.11.: Another seismogram: The direct wave and the reflected waves arrive at the receiver without any time-difference.

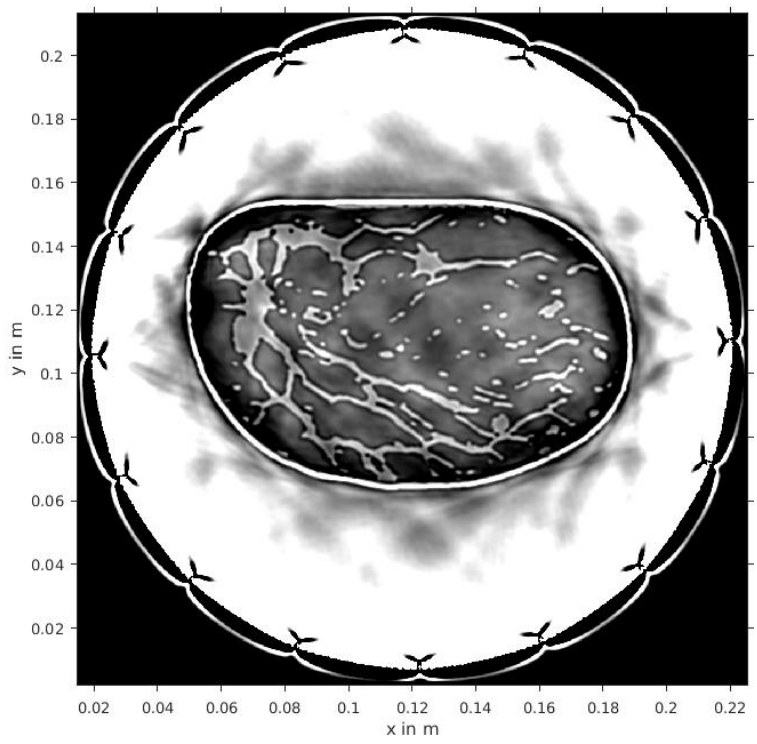

Figure 4.12.: Result of the reverse-time migration imaging after removing the transmitted wave.

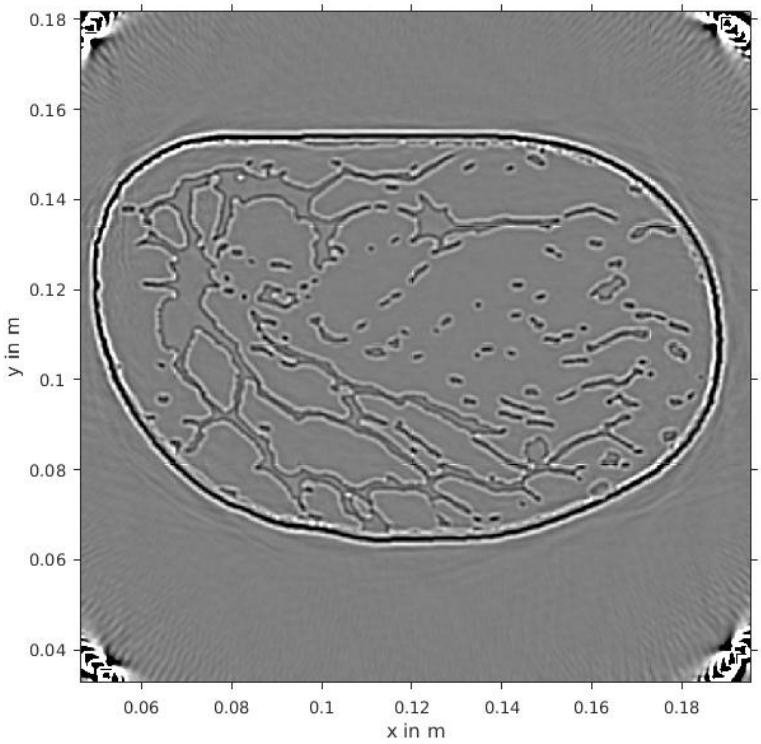

Figure 4.13.: Laplacian-filtered result after removing the transmitted wave.

However, a look at the details in figure 4.15 reveals that the image obtained with reverse-time migration with the full seismic data is sharper: Unmodified seismic data reproduce the shape and size of the tiny structures that can be found at the top right of the left image 4.15. The estimation of the size of tiny structures is more difficult if the direct waves are removed (right image). The measured line width follows this observation: While it amounts only two pixels in the original image, it widens to five with the modified seismograms. This is an unexpected result, since the direct waves do not contribute to the reflector mapping (see section 3.3) and therefore removing them should not affect the depiction of the reflectors. A possible explanation lies within the measurement setup, which consists of a circular arrangement of sources and receivers. This means, that some of the reflectors lie very close to the straight path from source to receiver, which is illustrated in figure 4.14. This might lead to an interference of the reflected wave with the direct wave, which is confirmed by the observation at the seismogram in figure 4.11, where no time-difference between the arrival of the direct (transmitted) wave and the reflections can be measured. Thus removing the direct wave might delete some information required for imaging.

Consequently, the question if the direct wave should be removed from the data is a question of other application conditions. Due to the possible interference of the direct wave with the reflected waves, the method with which the direct wave is removed from the data has to be considered carefully. A good fidelity of the data set allows to make use

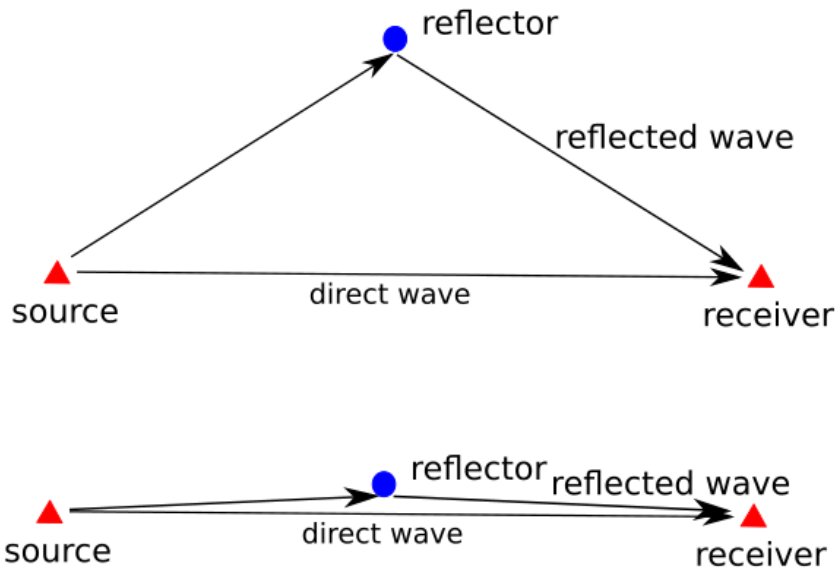

Figure 4.14.: The effect of the measurement setup: If the reflector lies apart from the straight path from source to reflector, the direct wave and the reflected wave can be separated. If the reflector lies close to the propagation path of the direct wave, the reflected and direct wave interfere.

of the additional information contained in the transmitted wave. The result is an image with an impressive granularity.

Removing the direct wave might be reasonable if the seismic data are very noisy. Due to the high amplitude of the direct wave there is a strong correlation between the transmitted wave and the noise. Thus, removing the direct wave should significantly reduce the noise in the image and improve its quality. This idea is being tested in section 4.7.3.

4.7. The effect of the medical measurement environment on the migration

A study with synthetic data by Roy et al. (2016) on reverse-time migration for breast screening demonstrates that this migration method is capable to image the female breast on perfect general conditions. Since no other study on this topic is published so far, the effect of conditions as they occur in ultrasound medical imaging is not known. The following numeric experiments determine how the measurement environment affects the migration result.

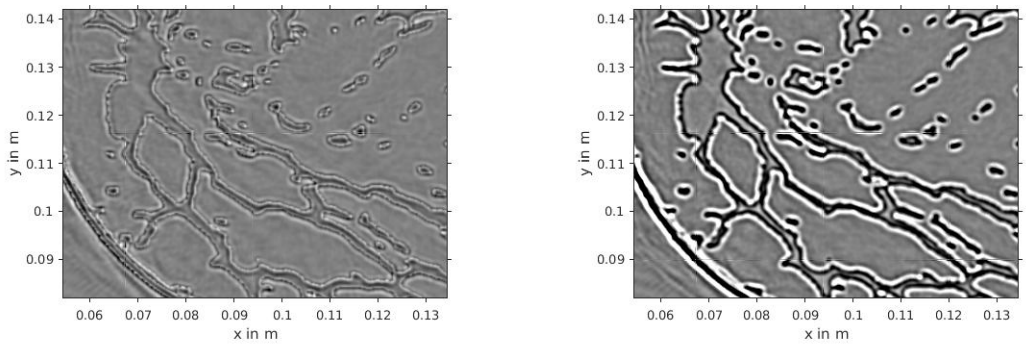

Figure 4.15.: A detailed look at the images obtained with reverse-time migration. Left: Result using full seismograms including the transmitted wave. Right: Result after modification of the seismograms by attenuating the transmitted wave

4.7.1. Model uncertainties

An important issue for real applications of reverse-time migration is that it requires a velocity and density model. A model can be obtained with the inversion methods described in chapter 2.4.1. Unfortunately, some of these algorithms have a very high computational cost. The results of some of them are used as an input model for the reverse-time migration. These experiments aim at determining which of the algorithms provide a velocity model that is sufficiently precise to obtain sharp results with reverse-time migration.

Smoothed reference model

Smoothing the model 4.1 might smooth the resulting image, because the traveltime changes slightly, also depending upon the direction the waves come from. Due to that the wavefields correlate at slightly different places.
The effect of very smooth models is examined with a constant velocity model and the bent-ray reconstruction model (see below). In order to find out how small changes in the velocity model affect the results, the reference-models are smoothed by a two-dimensional convolution with constant square kernels of different size up to 13 pixels, which corresponds to a physical size up to 2.6 mm. Figure 4.16 shows the resulting velocity model. It can be seen that this smoothing level smears the interfaces between two media, but most structures maintain. Then, the seismograms resulting from the reference model are migrated with a smoothed reverse-time migration input-model.
A comparison of the obtained images using the quality estimators is given in tabular 4.1 and plotted in figure 4.17. A detailed look at the image with the smoothest model of the experiments with a corresponding smoothing size of 2.6 mm is illustrated in figure 4.18.
A visual comparison shows that the sharpness is slightly reduced. The number of false positives is slightly increased linearly by increasing the size of the smoothing kernel (figure 4.17). At this point it is important that the gradient and the absolute numbers depend upon the chosen threshold of imaging energy for a reflection. In this case, the threshold is chosen arbitrarily in a way that the number of true positives is 11200 of 17620. This

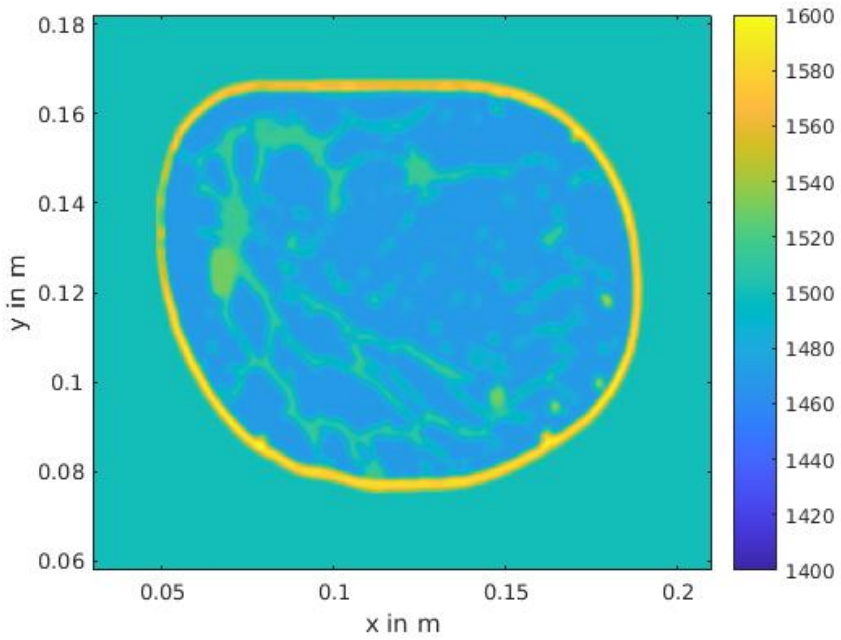

Figure 4.16.: The smoothed velocity model, created by convolving the reference model two-dimensionally with a thirteen pixel (corresponding to a physical size of 2.6 mm) constant square. Values in m/s.

Table 4.1.: Smoothed reverse-time migration model: Length of the smoothing average kernel, data of the confusion matrix and line width

Kernel	True +	False +	False -	True -	true/false	width
1	33451	21724	15641	1369184	0.47	2
5	33449	21726	21578	1363247	0.64	5
7	33489	21686	18151	1366674	0.54	6
9	33489	21686	19989	1364836	0.60	6
11	33501	21674	22078	1362747	0.66	6
13	33484	21691	23856	1360969	0.71	7

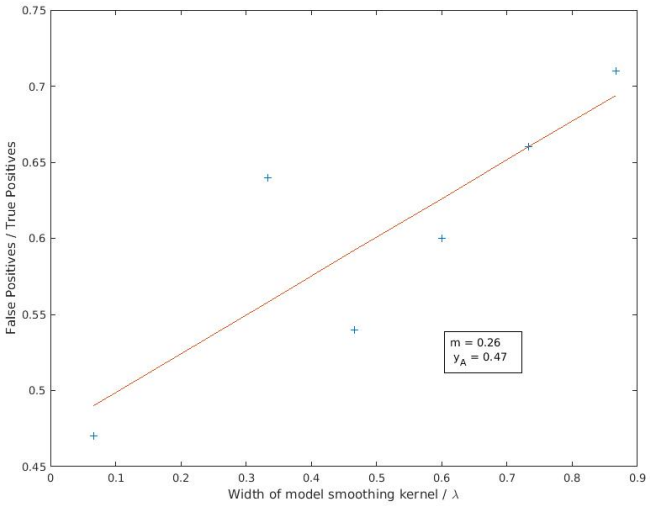

Figure 4.17.: Comparison of the false positives per true positives to the length of the smoothing kernel. The orange line is the linear regression with gradient m and y-intercept y_A.

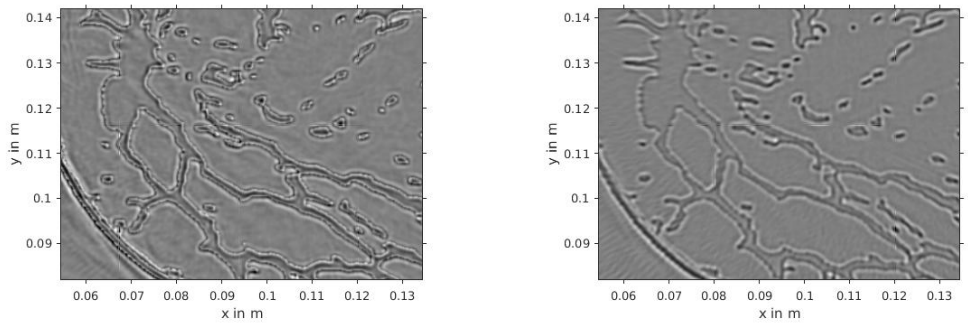

Figure 4.18.: A detailed look at the results of the reverse-time migration using different input models. Left: Reverse-time migration with the reference model. Right: Reverse-time migration with convolution of the reference model with a constant 13 pixel square.

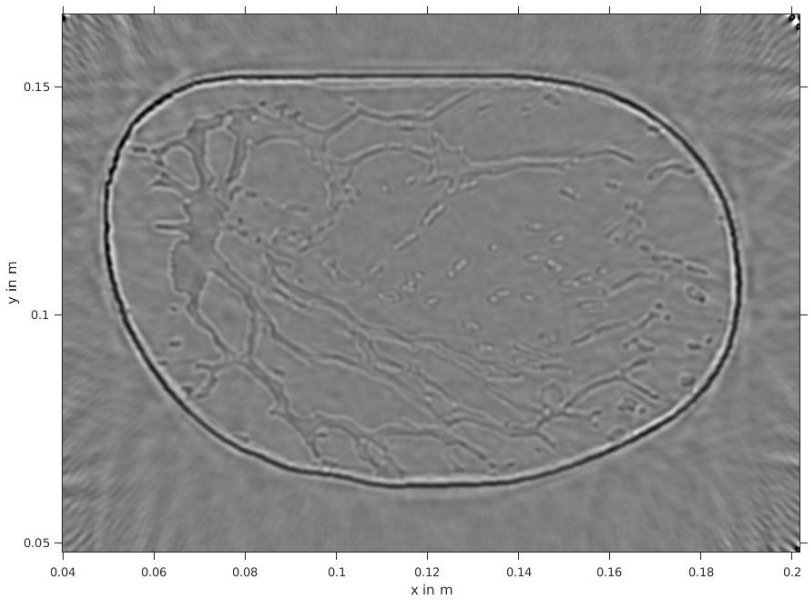

Figure 4.19.: Reverse-time migration with a homogeneous water model. Even though the contrast and sharpness is significantly reduced, it is still possible to localize all structures.

means that almost all reflecting structures can be identified, especially the tumor structure next to the fat, but not on the other side next to the fibroglandular tissue.
The linear regression turns out a gradient of 0.066 on the ratio of false per true positives per length of the smoothing kernel, which corresponds to an increase of 3.5%. The sharpness of the image is reduced slightly as the lines become wider from a width of 0.8 mm (four pixels) to a width of 1.4 mm (seven pixels) for kernels with a size of 0.6 mm and 2.6 mm (three and 13 pixels), respectively.
This result does not fit to the visual valuation. The image still looks sharp and does allow to describe the contours of all structures. Hence, it should be possible to obtain reasonable results with smooth input models.

Constant velocity model

The easiest model has a constant velocity and density that equal the corresponding water values. The migration of the seismic data is performed on such a model with a velocity of 1500 m/s and a density of 1000 kg/m^3. Figure 4.19 shows the results. The water-breast interface is mapped very sharp. This is an expected result, since the constant-velocity model is true between the transducers and the breast. Inside the breast, the contrast and the sharpness is reduced significantly. It is still possible to see all structures bigger than approximately half a centimeter. Smaller structures are still visible, but less highlight from the background.
The image can probably be improved with further image processing techniques that optimize the contrast of the image. The result demonstrates that reverse-time migration is very robust against inaccuracies in the velocity and density model. It might be possible

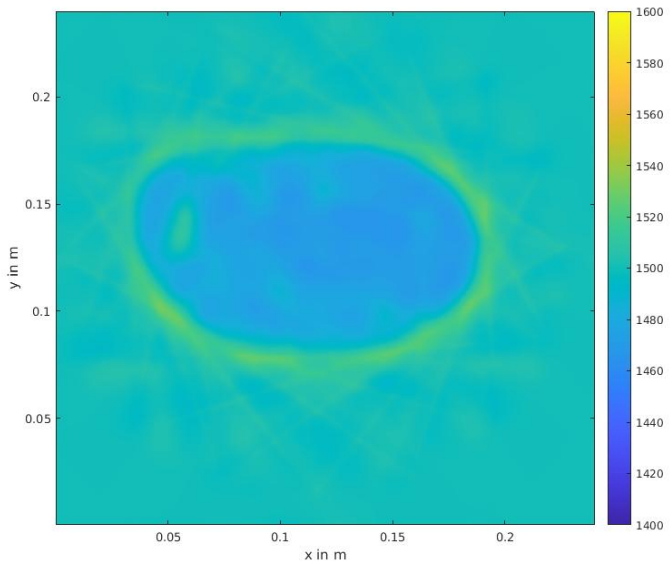

Figure 4.20.: Result of the bent-ray reconstruction in m/s with a source frequency of 500 kHz. This model serves as an input model for reverse-time migration.

to create a set of models that are good enough to migrate the measured data in a field application without further tomography, which significantly reduces the computational cost.

Reverse-time migration with bent-ray reconstruction

One of the easiest reconstruction methods to find an adequate velocity model is the bent ray reconstruction (see chapter 2.4.1). The tomography of the reference model with synthetic seismic data produces the model illustrated in figure 4.20. The reverse-time migration with this input model results in the reflectivity map 4.21. Compared to the result of the migration with the reference model, figure 4.7, the images' sharpness is reduced. Nevertheless, all structures are visible very well. The good image quality along with the low computational effort of the bent-ray reconstruction recommend this method to obtain the input model. Reverse-time migration combined with bent ray reconstruction produces granular images.

Reverse-time migration with full-waveform inversion

Full-waveform inversion is another possibility to compute a velocity model (see section 2.4.1). This method leads to the velocity model in figure 4.22. This model is very precise and equals the reference model up to a few meters per second. Since the model is accurate it is expected that reverse-time migration produces a result that is very similar to the result of the reference model. With this model, reverse-time migrations produces image 4.23. The expectation is confirmed. However, the computational effort of full-waveform inversion limits its practical use in the context of ultrasound medical imaging. The good

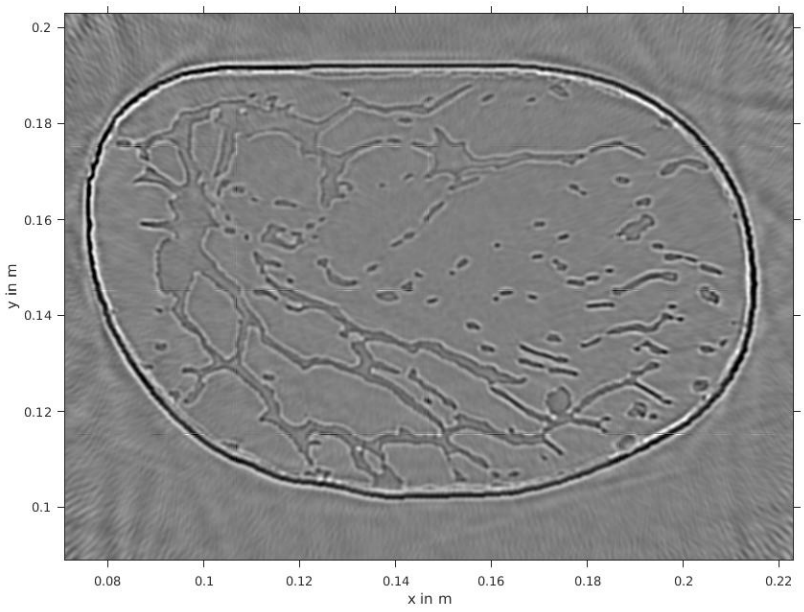

Figure 4.21.: Result of reverse-time migration using the bent-ray model.

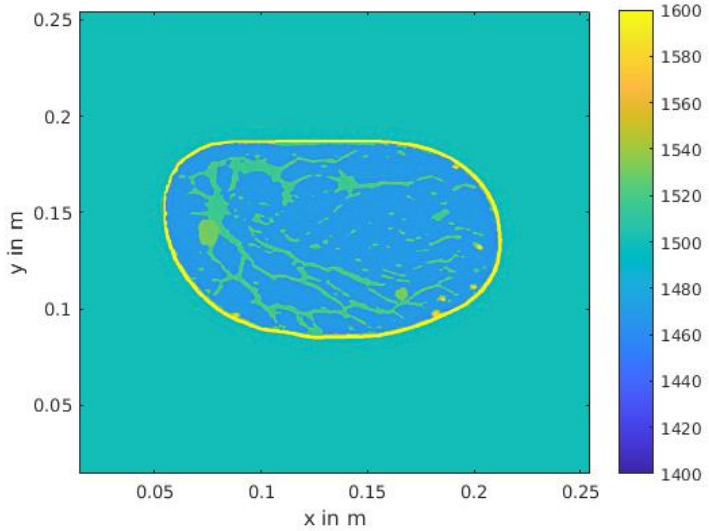

Figure 4.22.: Result of the full-waveform inversion. This model serves as an input model for the reverse-time migration.

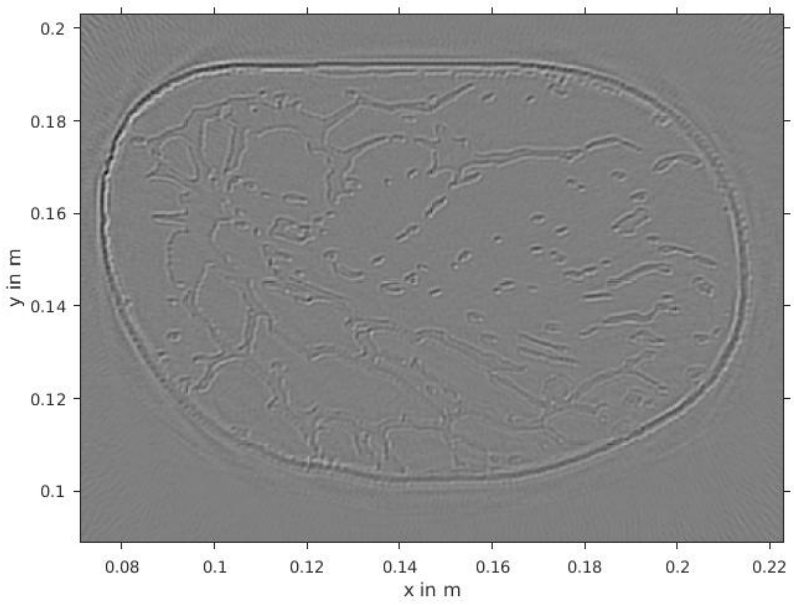

Figure 4.23.: Result of reverse-time migration using the full-waveform inversion model.

results of the bent-ray reconstruction recommend the latter method to obtain an input model for reverse-time migration.

4.7.2. Simulation of body movement

The patient is lying face down and immerses her breast into the ultrasound aperture. She should lie still, but since the data acquisition takes eight minutes for one breast (Ruiter et al., 2016), she might move slightly, for example due to breathing.
In order to simulate the movement of the breast, the model is shifted randomly with a Gaussian distribution for every shot. The mean shift in x- and y-direction amounts to 2 mm, which is approximately six times the wavelength and 1.2 % of the size of the breast. Then the synthetic seismograms are computed. These data are migrated with the reference model. The result is illustrated in figure 4.24. The movement has a big effect on the result. The image contains a matrix of confusing unordered lines, which are, probably, the overlap of slightly shifted images of the breast. It is impossible to make a difference between lines that describe a physical structure and lines that are movement artifacts. Reverse-time migration is very sensitive to body movement and solving the problem of these artifacts is a prerequisite for field reverse-time migration applications in medical imaging.
Since the wavefields need less than a millisecond to travel through the breast, the seismograms are barely affected by body movement and reconstructing only one shot should produce a sharp and shifted image of the breast. Consequently, a possible approach to reduce the movement artifacts might be to determine the location of the breast before the reverse-time migration by using all sources at the same time and the first registered

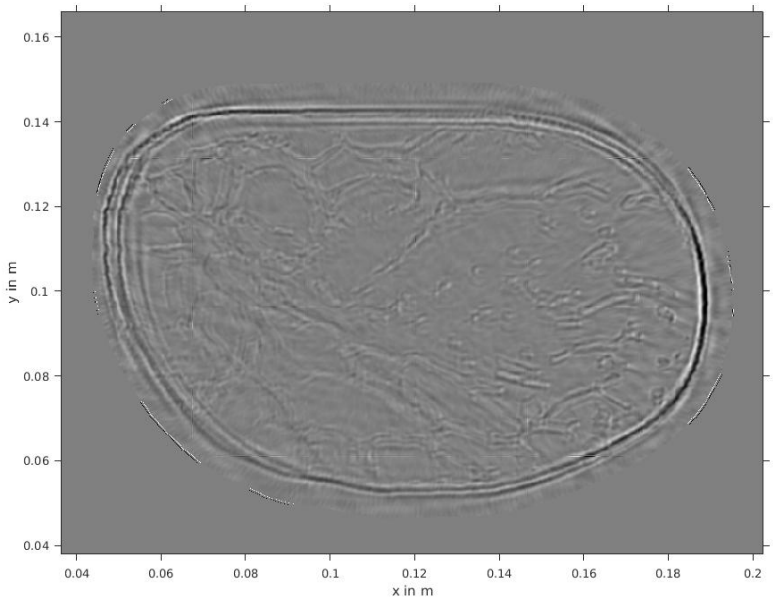

Figure 4.24.: Reverse-time migration with simulation of the body movement. The synthetic seismic data are calculated by shifting the model randomly for every shot. The migration uses the reference model.

reflection. These reflections are caused by the water-breast interface and might be used to locate the breast. Then the first transducer emits a wave and the data are collected. The obtained seismograms are shifted in a way that the arrival of their transmitted waves coincides with the arrival of the transmitted waves in the seismograms that have been measured for the localization of the breast. This procedure is repeated for all shots. Before starting the next shot, the breast is localized again. Then the reverse-time migration is applied for every shot individually. Methods using differential geometry then transform the breast contours with rotations and distortions to minimize the misfit between the breast illustrations of each shot. Stacking the images theoretically should result in a sharp projection.

4.7.3. Noisy data

Real measurements are contaminated by noisy signal contents. The effect of noise in the seismic data on the result of the reverse-time migration imaging is investigated quantitatively.
Therefore, Gaussian white noise is added to the seismograms obtained by forward modeling. In a field application, white noise is not realistic. For instance, the ultrasound signal is bandpass-filtered (Liu et al., 2007), which also affects the noise characteristics. Then the reverse-time migration is applied and the resulting images are evaluated as above.

Strong noise with a power of $-4\,\mathrm{dB}$ of the power of the seismograms causes a lot of artifacts. Circular wavefields around the sources partially overlap the water-breast interface and hide its structures. Details further away from the sources are easier to localize, even though the image is visibly noisy.

Table 4.2.: Image quality of noisy seismograms. Signal-to-noise ratio in dB of the power of the seismograms.

Noise	True +	False +	False -	True -	true/false +	Width	Noise in image
Inf	33451	21724	15641	1369184	0.47	2	Inf
44	33423	21752	15545	1369280	0.47	2	110
36	33420	21755	15613	1369212	0.47	2	98
28	33418	21757	15713	1369112	0.47	2	76
20	33401	21774	17015	1367810	0.51	2	59
12	33433	21732	32362	1352463	0.97	2	42
4	33412	21763	106802	1278023	3.2	1	24

Due to the cross-correlation imaging condition, imaging energy is computed everywhere where the transmitted wave has passed, overlapping the true structures.
In order to measure the strength of the noise in the image, the power of the original image is calculated by subtracting the mean of all pixels and then summing the squares of the imaging energy of all pixels. Afterwards, the image without noise is subtracted from the noisy image, so the remaining image only contains the noise. Its power is calculated the same way and then the two values are compared by calculating the signal-to-noise ratio in decibel of the power of the original image.
Table 4.2 presents the dependency of the image estimators on the noise levels. The reduced line width for strong noise is not surprising, since the auto-correlation of white noise converges to a delta distribution, hence its line width amounts to one. Obviously, this image sharpening does not involve an improvement in image quality.
The result indicates a linear relationship between the noise level in the input data and the noise level of the image. Reverse-time migration is evidently less susceptible to noise in the seismic data. Improving the signal-to-noise ratio by 10 dB lowers the noise in the image by 22 dB. This means that approximately $1/15.8 \approx 6\%$ of the noise in the seismic data are reproduced in the image. An interesting note is that this ratio equals the inverse of the number of sources. Recalculating the amplitudes from the power-ratio yields that the amplitudes of the imaging energy are approximately reduced by the root of the number of sources, which follows the general addition rules for white noise (Kallianpur, 1998).
The image produced with a signal-to-noise ratio of 12 dB has almost no quality loss. Even though the number of false positives already doubled, the visual effect is small (see figure 4.26). All structures can clearly be localized. In the case of a noise level of 4 dB the quality of the image (figure 4.26) significantly deteriorates through the presence of noise, but it is still possible to localize all tiny structures. However, in this case these structures hide inside the noise and finding them is very difficult. Hence, it is estimated that reverse-time migration can produce sufficiently detailed images of the model up to a seismic noise level of approximately $5 - 6$ dB.

Experiments with a removed direct wave (see chapter 4.6) yield that removing the transmitted wave leads to an improvement in image contrast and a reduction of the sharp-

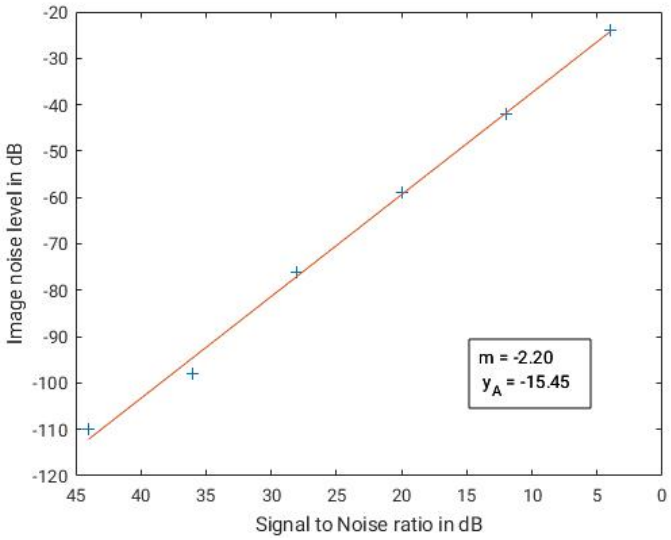

Figure 4.25.: Plot of the signal-to-noise ratio of the power of the image/the seismograms compared for different noise levels.

ness. An enhanced contrast should improve the image quality. Furthermore, the direct wave has the biggest amplitude, thus its correlation with the noise is responsible for a big amount of noise in the image. This assumption is examined in an experiment. At first, white Gaussian noise with a power of 4 dB of the power of the seismograms is added on the seismograms. Then the direct wave is attenuated and migrating the data produces image 4.27. The signal-to-noise ratio of the resulting image amounts to 20 dB, which is a worse result compared to the value with the full seismograms. The visual appearance is contradictory: The result is a strong improvement compared to figure 4.26. All structures can be visually localized again, verifying the assumption that removing the direct wave increases the image quality if the seismic data are noisy.

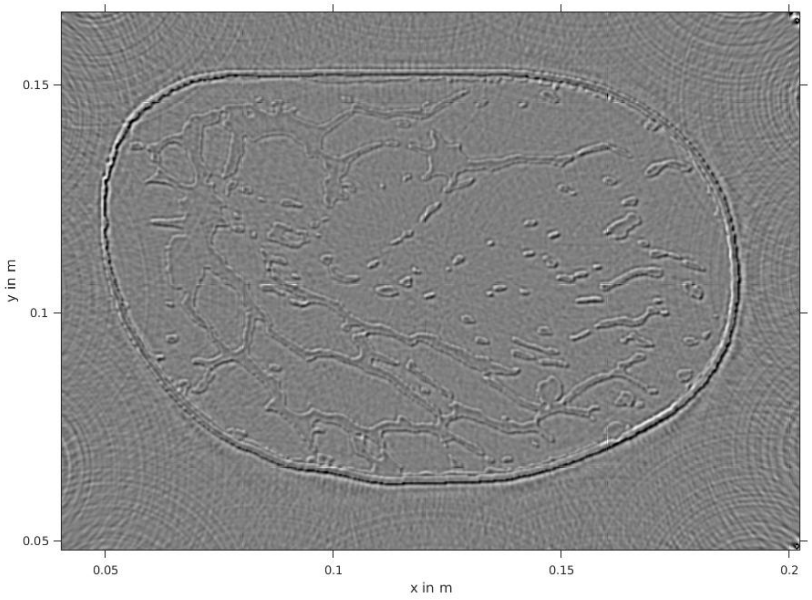

(a)

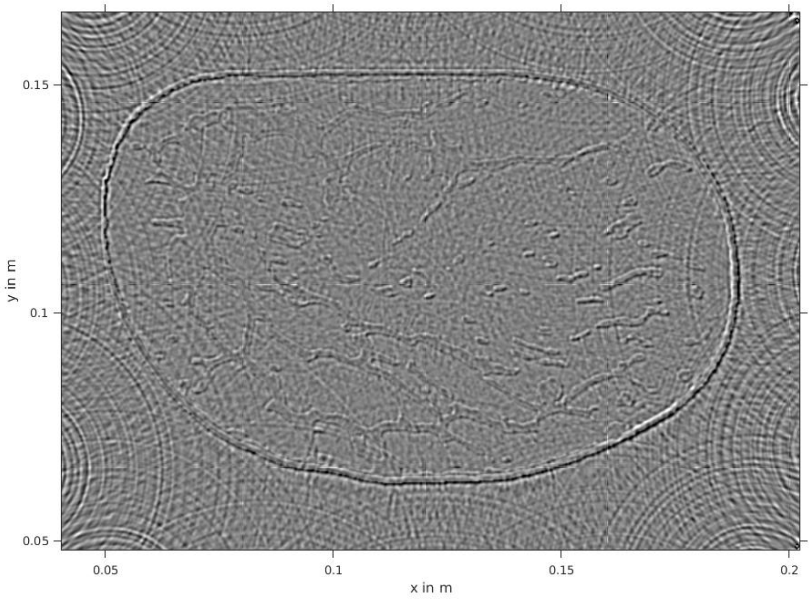

(b)

Figure 4.26.: Results after adding white Gaussian noise with a signal-to-noise ratio of the power of the seismograms of 12 dB (a) and 4 dB (b)

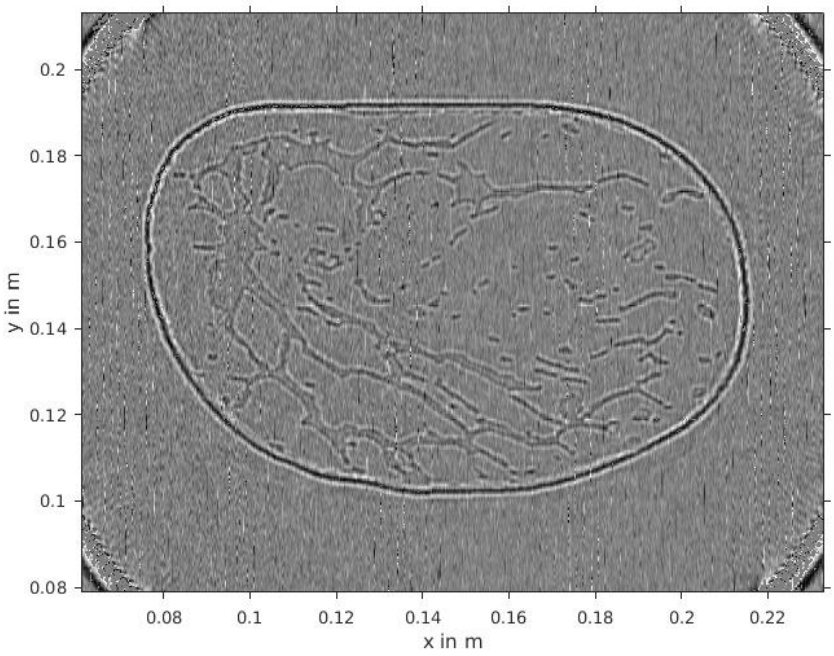

Figure 4.27.: Removing the transmitted wave at a signal-to-noise ratio of 4 dB clearly enhances the image quality

5. Conclusion

This thesis discussed that ultrasound imaging is a promising diagnostic technique for detecting breast cancer (section 2). The breast scanners are already available, for example at the USCT project in Karlsruhe. However, the image reconstruction is still an unsolved issue for the application. There already exist a number of algorithms, but they are either imprecise (e.g. the synthetic aperture focusing technique, section 2.4.2) or they are tomography algorithms with a computational effort that is too high for a reasonable field application.
At this point reverse-time migration is proposed for ultrasound image reconstruction (chapter 3). Solving the full wave-equation, in this case by a finite-difference approach, allows to take into account all wave phenomena.

The capabilities of this method have been tested on a synthetic model describing a female breast. 16 sources and 256 receivers that emit or record the acoustic waves surround the breast symmetrically.
The experimental results (chapter 4) demonstrate that reverse-time migration is capable to depict all structures very precisely even if the structures are very tiny. A comparison to a migration with the synthetic aperture focusing technique in section 4.5 yields a significant resolution gain and a reduction of image artifacts.
For an application in medical ultrasound imaging, different issues regarding the measurement environment have to be considered. Firstly, reverse-time migration requires a velocity model which has to be found before. Two possible algorithms to obtain such a model are the bent-ray reconstruction and the full-waveform inversion. The reverse-time migration is tested with velocity maps provided by these algorithms and with the assumption of constant velocity. The constant velocity model already yields an image that allows to localize most structures, but small structures almost vanish in the background since the image is not sharp enough for these details. With the other models, reverse-time migration produces granular images of the breast. Since the bent-ray reconstruction keeps the computational cost down, it is a reasonable algorithm for finding the required velocity map for reverse-time migration.
Secondly, reverse-time migration is robust to noise in the seismic data. In this case, only 6% of the power of the noise in the seismic data are reproduced in the image. If the ultrasound data are very noisy, removing the transmitted wave allows us to improve the image contrast while reducing the resolution.
A very important issue regarding reverse-time migration that has to be solved before the algorithm can be applied is body movement during the data acquisition. Otherwise movements of the breast will destroy the reconstruction of the image. Probably, the patient movement represents a universal problem that does not only occur for reverse-time migration, but also for all other reconstruction algorithms. Since the waves need less than

a millisecond to travel through the breast, the measurements of a single shot are barely affected by the movement and are expected to produce sharp, shifted images of the breast. Consequently, a numerical, geometrical correction of the breast position for each shot is expected to solve this problem.
In addition to that, the computational effort of reverse-time migration is still high. While a computation in the two dimensional case which has been performed in this study is still applicable, a possible three dimensional extension is a big challenge regarding the computer performance and its memory requirements. In a medical field application, the reverse-time migration should finish within some minutes, which is currently only possible with a huge IT infrastructure, if not impossible.

All in all, reverse-time migration is possibly the best breast ultrasound migration reconstruction technique, but only if sufficient computational resources are available.

Bibliography

Abubakar, A., Hu, W., Habashy, T. M., and van der Berg, P. M. (2009). Application of the finite-difference contrast-source inversion algorithm to seismic full-waveform data. *Geophysics*, 74 No.6.

Aiello, E., Buist, D., et al. (2004). Rate of breast cancer diagnoses among postmenopausal women with self-reported breast symptoms. *The Journal of the American Board of Family Practice*, 17, No.6.

Albert, U.-S. et al. (2008). Stufe-3-leitlinie brustkrebs- früherkennung in deutschland. *Universitätsklinikum Giessen und Marburg GmbH, W.Zuckschwerdt Verlag GmbH.*

Alsdorf, D. (1997). Noise reduction in seismic data using fourier correction coefficient filtering. *Geophysics*, 62 No.5.

American Cancer Society (2009). Cancer prevention, early detection facts and figures 2009. *American Cancer Society, Atlanta. pp34-37.*

Amin, V. R. (1989). Ultrasonic attenuation estimation for tissue characterization. *Iowa State University Digital Repository.*

Amstrong, K., Moye, E., Williams, S., Berlin, J., and Reynolds, E. (2007). Screening mammography in woman 40 to 49 years of age: A systematic review for the american college of physicians. *Annals of Internal Medicine; 146:516526.*

Carstensen, E. L. (1998). Absorption of ultrasound in tissues. *The Journal of the Acoustical Society of America*, 69, S3.

Claerbout, J. (1981). Toward a unified theory of reflector mapping. *Geophysics*, 36:467–481.

Courant, R., Friedrichs, K., and Lewy, H. (1928). Über die partiellen differenzengleichung der mathematischen physik. *Mathematische Annalen.*

Djarfour, N., Ferahtia, J., Babaia, F., Baddari, K., adj Said, E., and Farfour, M. (2014). Seismic noise filtering based on generalized regression neural networks. *Computers and Geosciences*, 69.

Duric, N. and Littrup, P. (2018). Breast ultrasound tomography. *IntechOpen.* `http://dx.doi.org/10.5772/intechopen.69794`, Viewed 10.09.2018.

Fledmann, M., Katyal, S., and Blackwood, M. (2009). Us artifacts. *Radiographics.*

Gemeinsamer Bundesausschuss (2017). Mammographie Screening. Eine Entscheidungshilfe. `www.g-ba.de/downloads`, Viewed 01.09.2018.

Guillermo, J. and Sierra-Sosa, D. (2016). Laguerre gaussian filters in reverse time migration image reconstruction. *VII Simpósio Brasileiro de Geofísica, 25 a 27 de outubro de 2016*. `pdfs.sematicscholar.org.`, Viewed 02.05.2018.

Guth, U., Huang, D., and Hober, M. (2008). Tumor size and detection in breast cancer: Self-examination and clinical breast examination are at their limit. *Cancer Detect Prev*, pages 224–228.

Haixia, U., Gao, J., and Chen, Z. (2014). Stability and numerical disperion analysis of finite-difference method for the diffusive-viscous wave equation. *International Journal of Numerical Analysis and Modeling, Series B.*, 5, No.1-2.

Han, B., He, Q., Chen, Y., and Dou, Y. (2014). Seismic waveform inversion using the finite-difference contrast source inversion method. *Journal of Applied Mathematics, Article ID 532159*.

Hardt, M., Ruiter, N., and Gemmeke, H. (2012). Analysis of the influence of multiple scattering on the reconstruction of ultrasound tomography signals using synthetic aperture focussing technique. 19th International Conference on Systems, Signals and Image Processing (IWSSIP).

Holberg, O. (1987). Computational aspects of the choice of operator and sampling interval for numerical differentiation in large-scale simulation of wave phenomena. *Geophysical Prospecting*, 35:629–655.

Hormati, A., Jovanović, I., Roy, O., and Vetterli, M. (2010). Robust ultrasound travel-time tomography using the bent ray model. *Proc. SPIE, Medical Imaging 2010: Ultrasonic Imaging, Tomography, and Therapy*, 7629. DOI: 10.1117/12844693.

Institut für Prozessdatenverarbeitung und Elektronik, KIT (2018). Brustkrebsfrüherkennung durch ultraschalltomographie. `https://www.ipe.kit.edu/167.php`, Viewed 03.09.2018.

Jiang, W., Liu, Z., and Zhang, J. (2017). Diffraction imaging using reverse time migration with poynting vectors. *SEG Technical Program Expanded Abstracts 2017*. doi: 10.1190/segam2017-17683099.1.

Jones, I. F. (2014). Tutorial: migration imaging conditions. *First break*, 32.

Kallianpur, G. (1998). White noise theory of prediction, filtering and smoothing. *CRS Press Inc.*

Köhn, D. (2011). Time domain 2d elastic full waveform tomography. Dissertation, Christian-Albrechts university, Kiel.

Komatitsch, D. and Martin, R. (2007). An unsplit convolutional perfectly matched layer improved at grazing incidence for the seismic wave equation. *Geophysics*, 72(5):155 – 167.

Kuan, D., an dT.C. Strand, A. S., and Chavel, P. (1985). Adaptive noise smoothing filters for images with signal-dependent noise. *IEEE Transactions on Pattern Analysis and Machine Intelligence*, 2.

Köhn, D., Nil, D. D., Kurzmann, A., Przebindowska, A., and Bohlen., T. (2012). On the influence of model parameterization in elastic full waveform tomography. *Geophysical Journal International*, 191(1):325–345.

Lee, D. and Shin, C. (2011). The direct-arrival-removal method of waveform inversion in the laplace domain for a deep-water model. *Journal of Seismic Exploration, 20.*

Liang, Z.-P. and Lauterbur, P. C. (1999). Principles of magnetic resonance imaging: A signal processing perspective. *Wiley.* ISBN 978-0-7803-4723-6.

Liu, F., Zhang, G., Morton, S. A., and Leveille, J. P. (2007). An effective imaging condition for reverse-time migration using wavefield decomposition. *Geophysics*, 71, No.1.

Liu, F., Zhang, G., Morton, S. A., and Leveille, J. P. (2011). An effective imaging condition for reverse-time migration using wavefield decomposition. *Geophysics*, 76:29–39.

Lou, Y., Zhou, W., Matthews, T. P., Appleton, C. M., and Anastasio, M. A. (2017). Generation of anatomically realistic numerical phantoms for photoacoustic and ultrasonic breast imaging. *Journal of Biomedical Optics*, 22.

Moss, C., Teixeira, F. L., and Kong, J. A. (2002). Analysis and compensation of numerical dispersion in the fdtd method for layered, anisotropic media. *IEEE Transactions on Antennas and Propagation*, 50, No.9.

Müller, G. (2007). Theory of elastic waves. *Samizdat Press.*

Ozmen, N. (2014). Ultrasound imaging methods for breast cancer detection. *Dissertation, Technische Universiteit Delft.*

Ozmen, N., Dapp, R., Zapf, M., and vad Dongen, K. (2015). Comparing different ultrasound imaging methods for breast cancer detection. *IEEE transactions on ultrasonics, ferroelectrics, and frequency control*, 62(4):637–46.

Rhiem, K. and Schmutzler, R. (2015). Risikofaktoren und prävention des mammakarzinoms. *Onkologe. doi:10.1007/s00761-014-2837-5.*

Robert Koch Institut (2018). `www.krebsdaten.de/Krebs/DE/Content/Krebsarten/Brustkrebs/brustkrebs_node.html`, Viewed 02.05.208.

Ross, Z. and Ben-Zion, Y. (2014). Automatic picking of direct, p, s seismic phases and fault zone head waves. *Geophysical Journal International*, 199.

Roth, M. Y., Elmore, J. G., and Miglioretti, D. L. (2011). Self-detection remains a key method of breast cancer detection for u.s. women. *Journal of Womens Health*, pages 1135–1139.

Roy, O., Zuberi, M., Pratt, R., and Duric, N. (2016). Ultrasound breast imaging using frequency domain reverse time migration. *Proceedings of the SPIE*, 9790.

Ruiter, N., Hopp, T., Zapf, M., Gemmeke, H., and Kretzek, E. (2016). Analysis of patient moving during 3D USCT data acquisition. *Conference paper*.

Ruiter, N. V., Zapf, M., Hopp, T., Gemmeke, H., and van Dongen, K. W. (2017). Usct data challenge. *Proc. of SPIE*, 10139.

Rumack, C. M., Wilson, S. R., Charboneau, J. W., and Levine, D. (2011). Diagnostic ultrasound. *Mosby*.

Sandhu, G., Li, C., Roy, O., Schmidt, S., and Duric, N. (2015). Frequency domain ultrasound waveform tomography: Breast imaging using a ring transducer. *Physics in Medicine and Biology*, 60 no.14.

Sava, P. and Fomel, S. (2003). Angle-domain common image gathers by wavefield continuation methods. *Geophyics*, 68, No.3.

Scheben, R. (2012). Algorithmen zur 3D-Ultraschall Rekonstruktion. Dissertation at the university of Saarland.

Sehgal, C. M., Weinstein, S. P., and Conant, E. F. (2006). A review on breast ultrasound. *Journal of Mammary Gland Biology and Neoplasia*.

Shin, C. (2003). One way vs two way wave equation imaging-is two-way worth it? *Research Gate*. `https://www.researchgate.net/profile/Changsoo_Shin/publication/280734110_One_Way_Vs_Two_Way_Wave_Equation_Imaging-Is_Two-Way_Worth_It`, Viewed 14.09.2018.

Skinner, K., Silbermann, H., and Silverstein, M. (2001). Palpable breast cancers are inherently different from nonpalpable breast cancer. *Ann Surg Oncol.*

Spiegel Online (2017). Welches Verfahren kann was? *Spiegel Online am 28.03.2017*. `www.spiegel.de/gesundheit/diagnose/brustkrebs-frueherkennung-durch-mammografie-ultraschal-und-mrt-a-1138038.html`, Viewed 12.09.2018.

United States Naval Academy (2017). Waves and the One-Dimensional Wave Equation. `www.usna.edu/Users/physics/ejtuchol/documents/SP411/Chapter2.pdf`,Viewed 20.09.2018.

W. Wang, T., Yokozeki, Ishijima, R., Takeda, M., and Hanson, S. (2006). Optical vortex metrology based on the core structures of phase singularities in laguerre-gauss transform of a speckle pattern. *Optics Express*, 14.

Zhou, H. W., Hu, H., Zou, Z., and Youn, O. (2018). Reverse time migration: A prospect of seismic imaging methodology. *Earth-Science Reviews*, 179.

A. Appendix

A.1. Implementation

The reverse-time migration has been implemented in the IFOS2D program. IFOS2D is free software: it can be redistributed and/or modified it under the terms of the GNU General Public License as published by the Free Software Foundation, version 2.0 of the License only. The software is available at the corresponding website, https://git.scc.kit.edu/GPIAG-Software/IFOS2D.

IFOS2D performs a full-waveform inversion with the scheme presented in section 2.4.1. The reverse-time migration has been implemented by skipping the forming of the residuals $\delta\vec{u}$ (step 3), and then back-propagating the full time-reversed seismograms instead of the data residuals in step 4. The cross-correlation (step 5) yields the result of the migration. Then the program aborts.

A.2. Source positions

The source positions are listed in table A.1.

Table A.1.: Source positions in the numerical experiments

x in m	y in m	x in m	y in m
0.108	0.2056	0.1462	0.197
0.178	0.1746	0.1988	0.1416
0.2056	0.1032	0.197	0.065
0.1746	0.0332	0.1416	0.0124
0.1032	0.0056	0.065	0.0142
0.0332	0.0366	0.0124	0.0696
0.0056	0.108	0.0142	0.1462
0.0366	0.178	0.0696	0.1988